

# Revisiting the Fermionic Dark Matter Absorption on Electron Target

Shao-Feng Ge,<sup>1,2,\*</sup> Xiao-Gang He,<sup>1,3,†</sup> Xiao-Dong Ma,<sup>1,2,‡</sup> and Jie Sheng<sup>1,2,§</sup>

<sup>1</sup>*Tsung-Dao Lee Institute (TDLI) & School of Physics and Astronomy (SPA),  
Shanghai Jiao Tong University (SJTU), Shanghai 200240, China*

<sup>2</sup>*Key Laboratory for Particle Astrophysics and Cosmology (MOE)  
& Shanghai Key Laboratory for Particle Physics and Cosmology,  
Shanghai Jiao Tong University, Shanghai 200240, China*

<sup>3</sup>*Department of Physics, National Taiwan University, Taipei 10617*

We perform a systematic study of the fermionic DM absorption interactions on electron target in the context of effective field theory. The fermionic DM absorption is not just sensitive to sub-MeV DM with efficient energy release, but also gives a unique signature with clear peak in the electron recoil spectrum whose shape is largely determined by the atomic effects. Fitting with the Xenon1T and PandaX-II data prefers DM mass at  $m_\chi = 59$  keV and 105 keV, respectively, while the cut-off scale is probed up to around 1 TeV. The DM overproduction in the early Universe, the invisible decay effect on the cosmological evolution, and the astrophysical X(gamma)-ray from the DM visible decays are thoroughly explored to give up-to-date constraints. With stringent bounds on the tensor and pseudo-scalar operators, the other fermionic DM operators are of particular interest at tonne-scale direct detection experiments such as PandaX-4T, XENONnT, and LZ.

## I. INTRODUCTION

The nature of dark matter (DM) remains a mysterious puzzle in our understanding of the Universe [1, 2]. The possible particle characteristic of DM is a well-motivated scenario to be probed by the direct detection experiments [3, 4] and indirect observations [5, 6]. The stability of DM particle is usually realized by some discrete symmetry such as  $\mathbb{Z}_2$  [7–9]. A direct consequence is that in direct detection, the scattering process has a DM particle in the initial state and another DM particle in the final one. The energy deposit comes from the DM kinetic energy. With typical experimental threshold at  $\mathcal{O}(1)$  keV, direct detection experiments are only sensitive to the DM mass above GeV. In the GeV~TeV mass range, the null result from the direct detection experiments has put very strong limit on the DM interaction strength with the Standard Model (SM) particles [10, 11]. In contrast, the cross section of sub-GeV light DM scattering with SM particles is much less stringently constrained and can still be large [3, 4]. More attention has been turned to light DM alternatives with sub-GeV mass [12] or even lighter ones such as the sterile neutrino DM [13–16].

However, one difficulty for the light DM detection is its small recoil energy. For a typical DM scattering with nuclei target, the recoil energy  $T_r = 4m_\chi m_A T_\chi / (m_\chi + m_A)^2$  is proportionally scaled from the DM kinetic energy  $T_\chi$ . The most efficient energy transfer happens when the DM mass  $m_\chi$  is roughly the size of the atomic mass  $m_A$  of the nuclei target,  $T_r \approx T_\chi$ . With light DM,  $m_\chi \ll m_A$ , the recoil energy  $T_r \approx 4m_\chi T_\chi / m_A$  decreases with not just the DM mass  $m_\chi$  but also its kinetic energy  $T_\chi$ . More importantly, the DM kinetic energy is also proportional to its mass,  $T_\chi \approx \frac{1}{2}m_\chi v_\chi^2$ , while the distribution of its velocity  $v_\chi$  is fixed by the galaxy gravitational potential [17]. Altogether, the nuclear recoil from the light DM scattering scales with  $m_\chi^2$ . This explains why the direction detection sensitivity deteriorate fast in the sub-GeV range. It is desirable to find possible ways to overcome this difficulty.

---

\* gesf@sjtu.edu.cn

† hexg@phys.ntu.edu.tw

‡ maxid@sjtu.edu.cn

§ shengjie04@sjtu.edu.cn

There are several ways of improving the detection of light DM. For nuclear recoil, the detection threshold can be lowered by using Germanium point-contact detector [18], bolometer [19, 20], nuclear bremsstrahlung [21, 22], and Migdal effect [22–33]. Or one may replace the nuclear recoil by electron recoil. Then, the elastic recoil energy is  $T_r = 4m_\chi m_e T_\chi / (m_\chi + m_e)^2$  which removes the suppression factor  $m_\chi/m_A$ . In addition to using the conventional detector for measuring the electron recoils, various new technology has been developed. From the condensed matter side, the typically small energy gap is of great advantage to build a low threshold detector such as using superheated liquid [34], super-conduction [35], Fermi degenerate materials [36], super-fluid [37], scintillation [38], magnetic molecular [39], Dirac material [40], diamond crystal [41], nanowire [42], nanotube [43], magnon [44], graphene [45], and plasmon [46]. In particular, a semi-conductor detector such as skipper CCD is very sensitive to single electron events [47]. The biological DNA also provides an interesting possibility [48].

On the other hand, DM particles upscattered to higher energy can also overcome the detection threshold. Several possibilities have been discussed in the literature. The nonrelativistic DM particles can be boosted by the cosmic rays to gain sufficient energy [49–64]. This cosmic ray boosted DM (CRDM) scenario can happen as long as DM interacts with SM particles which is exactly the foundation of DM direct detection. Actual experimental search with real DM direct detection data has been carried out by PandaX-II [65] and CDEX [66], in addition to those constraints from neutrino experiments [51, 67–71] and indirect constraints [49, 72]. The CRDM may also be produced by astrophysical neutrinos [73–78] and blazar [79]. If the DM particle is light enough, it is also possible for them to be produced by the cosmic ray interactions with the atmosphere [80–82]. Another place to boost light DM is the Sun [83–88]. With multiple components, the boosted light DM can also happen inside the dark sector [89–93].

Another possibility is the fermionic DM absorption. The upscattered DM scenarios mentioned in the above paragraph can probe light DM, but the dependence on the DM mass may not be significant. This is because smaller mass usually means smaller effect on the kinematics, especially if DM particles are highly boosted. In order for DM detection to be sensitive to the light DM mass, the mass term should dominate the relevant kinematics. Namely, non-relativistic DM may have some advantage in this regard. If a nonrelativistic DM releases all its mass into energy, its mass is the dominant factor and the detection threshold can also be overcome with efficient amplification by the speed of light,  $E = mc^2$ . This is exactly the idea of DM absorption for bosonic [94–102] and fermionic [103–105] DM.

This paper is organized as follows. In Sec. II, we introduce the motivation for the sub-MeV fermionic absorption DM and enumerate all the possible effective absorption operators. In Sec. II A we discuss the signal in direct detection experiment. Then we evaluate the constraints from DM overproduction of the early Universe in Sec. III as well as the cosmological evolution constraint on the invisible decay  $\chi \rightarrow 3\nu$  and astrophysical constraints with X(gamma)-rays on the visible decay modes  $\chi \rightarrow \nu + \gamma(s)$  in Sec. V. More details about the calculation of DM decay is provided in Sec. IV. Our main results are summarized in Sec. VI. On the technical side, we provide simplified algorithms for a general-purpose analytic  $\chi^2$  fit with collective marginalization in App. A.

## II. SUB-MEV FERMIONIC ABSORPTION DM ON ELECTRON TARGET

As pointed out above, the light DM has intrinsic difficulty in the direct detection experiments due to energy threshold. One possible way of overcoming this comes from the fermionic DM absorption,  $\chi e \rightarrow \nu e$ , where the DM particle  $\chi$  scatters into a massless SM neutrino  $\nu$ . Placing neutrino in the final state not only conserves charge but also is the most economical choice to maximize the energy

release. Then the DM mass  $m_\chi$  is wholly converted to the electron recoil and neutrino energies. The fermionic DM absorption on a nuclei target is also possible [103, 104] but requires heavier DM above MeV mass to overcome the detection threshold. In our current paper, we focus on the electron target that is optimal for sub-MeV DM [105].

For a free electron target at rest, the electron recoil energy is  $T_r \approx m_\chi^2/2m_e$  [105], which is a good approximation for  $m_\chi \ll m_e$ . A keV scale DM can already produce large enough electron recoil energy to overcome the detection threshold that is typically 1 keV for the electron signal [106, 107]. Although larger electron recoil energy  $T_r$  is better for direct detection threshold, the DM mass is not larger the better. For  $m_\chi = 1$  MeV, the electron recoil approaches 1 MeV which may saturate the detector capability. So we focus on the sub-MeV DM mass range with  $1 \text{ keV} \lesssim m_\chi \lesssim 1 \text{ MeV}$  across this paper.

To make a systematic study of the fermionic DM absorption, we take the effective field theory (EFT) approach for a model independent analysis. As argued at the beginning of this section, the relevant degrees of freedom are the light SM particles, electron and neutrino, augmented with an additional DM particle. Usually, the SM gauge symmetries  $U(1)_Y \times SU(2)_L \times SU(3)_c$  is kept intact for an EFT approach. Nevertheless, the DM direct detection happens at low energy where the electroweak part is broken. Only the electromagnetic  $U(1)_{\text{em}}$  is a good symmetry to guide the construction of EFT operators as far as gauge symmetry of the theory is concerned. The strong interaction  $SU(3)_c$  is of no relevance since no color degrees of freedom are involved.

For the fermionic DM absorption on the electron target, the leading local interactions are dimension-six operators involving a dark matter particle  $\chi$ , an active SM neutrino  $\nu$  and an electron current,

$$\mathcal{O}_{e\nu\chi}^S \equiv (\bar{e}e)(\bar{\nu}_L\chi_R), \quad (1a)$$

$$\mathcal{O}_{e\nu\chi}^P \equiv (\bar{e}i\gamma_5e)(\bar{\nu}_L\chi_R), \quad (1b)$$

$$\mathcal{O}_{e\nu\chi}^V \equiv (\bar{e}\gamma_\mu e)(\bar{\nu}_L\gamma^\mu\chi_L), \quad (1c)$$

$$\mathcal{O}_{e\nu\chi}^A \equiv (\bar{e}\gamma_\mu\gamma_5e)(\bar{\nu}_L\gamma^\mu\chi_L), \quad (1d)$$

$$\mathcal{O}_{e\nu\chi}^T \equiv (\bar{e}\sigma_{\mu\nu}e)(\bar{\nu}_L\sigma^{\mu\nu}\chi_R), \quad (1e)$$

and their Hermitian conjugates. For completeness, we have considered all the five independent Lorentz structures for the electron bilinear (scalar [S], pseudo-scalar [P], vector [V], axial-vector [A] and tensor [T]). The neutrino field is taken to be the SM left-handed component  $\nu_L$  and the DM  $\chi$  is assumed to be a Dirac particle for convenience. Any other types of operators can be converted to those in (1) by Dirac gamma matrix identities and Fierz transformations [108–110]. For instance, the operator  $(\bar{e}\sigma_{\mu\nu}\gamma_5e)(\bar{\nu}_L\sigma^{\mu\nu}\chi_R)$  is equivalent to  $\mathcal{O}_{e\nu\chi}^T$  by the identities  $\sigma^{\mu\nu}\gamma^5 = \frac{i}{2}\epsilon^{\mu\nu\rho\sigma}\sigma_{\rho\sigma}$  and  $\gamma_5 P_R = P_R$  with  $P_R$  being the right-handed projection operator.

Each operator carries a Wilson coefficient  $C_i$ . Since the operators are already dimension 6,  $C_i \equiv 1/\Lambda^2$  carry two units of inverse mass dimension,  $[\text{mass}]^{-2}$ . Given new physics scenario, a heavy mediator can be integrated away to match the effective interaction. Equivalently, the effective scale  $\Lambda$  can be identified with the heavy mediator mass up to some dimensionless coupling constants. Although there is no fundamental principle to forbidden the above operators to simultaneously appear, we consider them separately in the following discussions.

### A. Fermionic DM Absorption on Electron and Atomic Effects

The local DM distribution around the Sun is roughly known from the hydrodynamic simulation of our Milky Way galaxy [17]. With the DM energy density,  $\rho_\chi \approx 0.4 \text{ GeV}/\text{cm}^3$ , its number density

$n_\chi = \rho_\chi/m_\chi$  is inversely proportional to mass  $m_\chi$ . In addition, the DM velocity distribution is determined by the gravitational potential of the galaxy matter and dark matter. Around the Sun, the DM velocity follows the Maxwell-Boltzmann distribution and peaks around typically  $v_\chi \sim (200 \sim 300)$  km/s. In other words, the DM in our solar system is non-relativistic with only  $\mathcal{O}(10^{-3})$  of the speed of light. Since the absorption process releases the whole DM mass as the energy of final-state particles, its kinetic energy  $T_\chi \approx \frac{1}{2}m_\chi v_\chi^2$  is negligibly small,  $T_\chi/m_\chi \sim \mathcal{O}(10^{-6})$ . We can take both the initial electron and DM particle as at rest to estimate the scattering cross section  $\sigma_{\chi e}$ ,

$$\sigma_{\chi e}^S v_\chi \approx \frac{1}{\Lambda^4} \frac{m_\chi^2 (2m_e + m_\chi)^4}{64\pi (m_e + m_\chi)^4}, \quad (2a)$$

$$\sigma_{\chi e}^P v_\chi \approx \frac{1}{\Lambda^4} \frac{m_\chi^4 (2m_e + m_\chi)^2}{64\pi (m_e + m_\chi)^4}, \quad (2b)$$

$$\sigma_{\chi e}^V v_\chi \approx \frac{1}{\Lambda^4} \frac{m_\chi^2 (2m_e + m_\chi)^2 (2m_e^2 + 4m_e m_\chi + 3m_\chi^2)}{32\pi (m_e + m_\chi)^4}, \quad (2c)$$

$$\sigma_{\chi e}^A v_\chi \approx \frac{1}{\Lambda^4} \frac{m_\chi^2 (2m_e + m_\chi)^2 (6m_e^2 + 8m_e m_\chi + 3m_\chi^2)}{32\pi (m_e + m_\chi)^4}, \quad (2d)$$

$$\sigma_{\chi e}^T v_\chi \approx \frac{1}{\Lambda^4} \frac{m_\chi^2 (2m_e + m_\chi)^2 (6m_e^2 + 10m_e m_\chi + 5m_\chi^2)}{8\pi (m_e + m_\chi)^4}. \quad (2e)$$

Those terms suppressed by the DM velocity  $v_\chi$  have been neglected for clarity. Nevertheless, the DM velocity does not disappear completely since the quantity that enters the DM event rate is  $\sigma_{\chi e} v_\chi$  as a whole. In the limit of tiny DM mass,  $m_\chi \ll m_e$ , all cross sections reduce to a universal value,  $m_\chi^2/4\pi\Lambda^4$  [105].

In reality, the initial and final electrons are subject to the Coulomb potential produced by the central nuclei and other surrounding electrons. There is no way for the initial electron that is confined inside the atom to be at rest. Not to say for a typical  $\mathcal{O}(\text{keV})$  electron recoil, its kinetic energy is of the same size as the binding energy. The atomic binding effect could be large enough to affect the direct detection event rate. We follow the general formalism developed with second quantization for both the initial bound and final ionized electron states [111]. The differential cross section is then a convolution of the particle scattering amplitude  $|\mathcal{M}|^2$  and the atomic  $K$ -factor  $K_{nl}(T_r, |\mathbf{q}|)$ ,

$$\frac{d\sigma_{\chi e}}{dT_r} v_\chi = \frac{1}{T_r} \sum_{nl} (4l+2) \int \frac{d^3\mathbf{q}}{(2\pi)^3 2E_\nu} \frac{1}{8m_e^2 E_\chi} |\mathcal{M}|^2(\mathbf{q}) K_{nl}(T_r, |\mathbf{q}|) (2\pi) \delta_E, \quad (3)$$

The summation over the principle quantum number  $n$  and the angular momentum  $l$  is a product of the electron number  $(2l+1)$  of the state  $|nl\rangle$  and the spin degree of freedom 2.

The remaining  $\delta_E$  function comes from energy conservation. For non-relativistic DM, its kinetic energy can be omitted in comparison with the energy release from the DM absorption process,

$$\delta_E \equiv \delta(m_\chi - |\mathbf{q}| - \Delta E_{nl}). \quad (4)$$

With vanishing mass, the neutrino energy  $E_\nu = |\mathbf{q}|$  is the same as its momentum and equivalently the size of momentum transfer  $|\mathbf{q}|$ . On the electron side, the energy gain,  $\Delta E_{nl} \equiv T_r - E_{nl}$ , is the difference between the ionized electron energy  $T_r$  and the negative initial binding energy  $E_{nl}$  for the state  $|nl\rangle$ . It is then desirable to first integrate  $|\mathbf{q}|$  away from the phase space element  $d^3\mathbf{q} = |\mathbf{q}|^2 d|\mathbf{q}| d\Omega_q$ . For the scattering with a bound electron,  $|\mathbf{q}|$  and  $T_r$  are usually independent variables due to the unknown initial electron momentum inside an atom. However, the energy conservation (4) establishes a correlation,  $|\mathbf{q}| = m_\chi - \Delta E_{nl}$ .

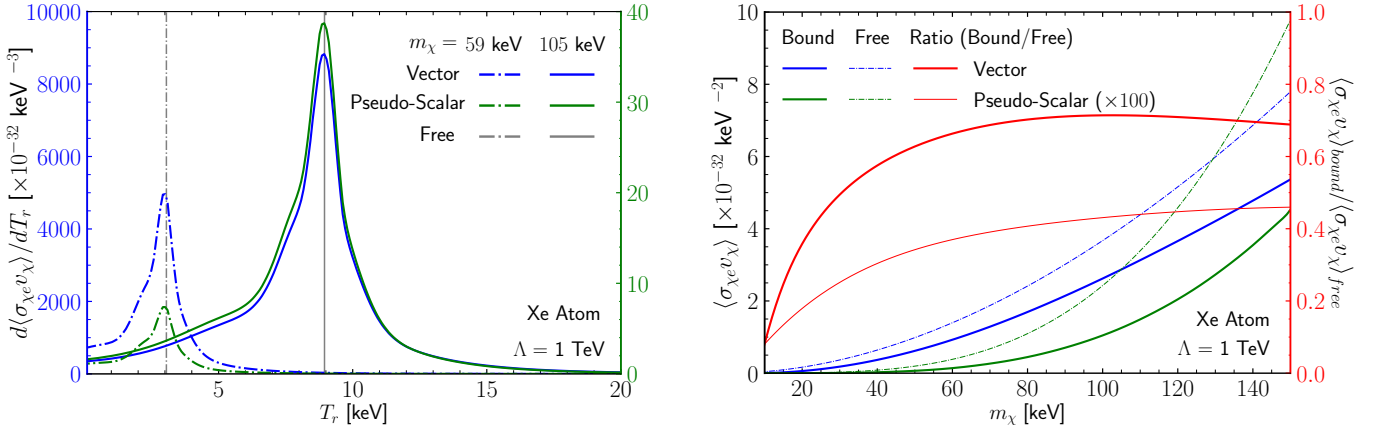


FIG. 1. **(Left)** The atomic effects of Xe on the electron recoil spectrum with two typical DM masses  $m_\chi = 59 \text{ keV}$  (dot-dashed) and  $105 \text{ keV}$  (solid) for vector (blue) and pseudo-scalar (green) operators. Since the pseudo-scalar cross section is sensitive to the DM mass, the left axis adopts a scale of  $\mathcal{O}(1000)$  in blue for the vector case while the right one of  $\mathcal{O}(10)$  in green for the pseudo-scalar one. **(Right)** The atomic effects on the thermally averaged total cross section with velocity weight  $\langle\sigma_{\chi e\nu_\chi}\rangle$  for vector (blue) and pseudo-scalar (pseudo-scalar) cases. Comparison has been made between the scattering cross section with a bound (thick) and free (thin) electron while the bound/free ratios are shown in red color according to the right axis scale.

On the other hand, the solid angle integration  $d\Omega_q \equiv d\cos\theta_q d\phi_q$  contains the information of momentum transfer direction. However, neither the  $K$ -factor  $K_{nl}(T_r, |\mathbf{q}|)$  [111] nor the scattering matrix element  $|\mathcal{M}(\mathbf{q})|^2$  has dependence on the angular coordinates of  $\mathbf{q}$ . For the latter, the angular independence happens due to the fact that the DM velocity is negligible in the absorption process. Without a preference, the direction of  $\mathbf{q}$  is not important either. The solid angle integration then simply gives an overall  $4\pi$ . Consequently, (3) becomes,

$$\frac{d\langle\sigma_{\chi e\nu_\chi}\rangle}{dT_r} = \sum_{nl} (4l+2) \frac{1}{T_r} \frac{m_\chi - \Delta E_{nl}}{16\pi m_e^2 m_\chi} |\mathcal{M}(\mathbf{q})|^2 K_{nl}(T_r, |\mathbf{q}|), \quad (5)$$

where we have implemented the facts that  $E_\nu = |\mathbf{q}|$  and  $|\mathbf{q}| = m_\chi - \Delta E_{nl}$ . Since the left-hand sides of (3) and (5) are independent of the DM velocity,  $\sigma_{\chi e\nu_\chi}$  is essentially  $\langle\sigma_{\chi e\nu_\chi}\rangle$ . Although there are five operators in (1), the scattering matrix element  $|\mathcal{M}|^2$  has only two different forms,

$$|\mathcal{M}^{(S,V,A,T)}|^2 = (4, 4, 12, 48) \times \frac{1}{\Lambda^4} m_\chi m_e^2 (m_\chi - \Delta E_{nl}), \quad |\mathcal{M}^P|^2 = \frac{1}{\Lambda^4} m_\chi (m_\chi - \Delta E_{nl})^3. \quad (6)$$

The pseudo-scalar (P) case is quite special since the matrix element intrinsically has momentum transfer dependence as elaborated in [111]. For comparison, the others have exactly the same structure.

The left panel of Fig. 1 shows the typical differential and total cross sections for  $m_\chi = (59, 105) \text{ keV}$ . Since the scalar, vector, axial vector, and tensor interactions share the same matrix element structure and consequently the same differential spectrum, only vector (blue) and pseudo-scalar (green) curves are shown. For comparison, the electron recoil energy from the DM absorption on a free electron at rest takes a fixed value (gray),  $T_r = m_\chi^2/2(m_e + m_\chi)$  which is derived without approximation. Although the spectrum widens due to atomic effect, the peak is still at exactly the same location as the free case. For  $m_\chi = (59, 105) \text{ keV}$ , the peak position is  $T_r = (3.05, 8.95) \text{ keV}$ , respectively. We have adjusted the  $y$ -axis scales for the vector (left blue) and pseudo-scalar (right green) cases to make the  $m_\chi = 105 \text{ keV}$  peaks with roughly the same height. Since the matrix element  $|\mathcal{M}|^2$  has  $m_\chi - \Delta E_{nl}$  dependence for the vector operator and  $(m_\chi - \Delta E_{nl})^3$  for the pseudo-scalar one, the  $m_\chi = 59 \text{ keV}$  peak heights scale accordingly. With major contribution coming from the outer shell electrons, the binding energy  $E_b = (0.16, 0.012) \text{ keV}$  for ( $4p, 5p$ ) shells can be negligibly small. Then

the peak height scales with  $m_\chi - T_r$  and  $(m_\chi - T_r)^3$ , respectively. For the vector (pseudo-scalar) case, the peak height reduces by a factor of 0.58 (0.20). This explains why the pseudo-scalar peak is only around 1/3 of the vector counterpart for  $m_\chi = 59$  keV. The  $T_r$  dependence arises from the  $K$ -factor and energy gain  $\Delta E_{nl} = T_r - E_{nl}$ . Although the  $m_\chi - T_r$  dependence is quite different, the spectrum shape has only slight difference among operators. This is because the two cases shown in the left panel of Fig. 1 has  $m_\chi \gg T_r$ . Consequently, the  $T_r$  spectrum is mainly determined by the  $K$ -factor which is universally shared. This allows a unique probe that is model-independent, or at least operator-independent, to some extent. Once detected, fermionic DM absorption even allows in-situ measurement of the atomic  $K$ -factor.

The right panel of Fig. 1 shows the total cross section  $\langle\sigma v_\chi\rangle$  as a function of the DM mass. With larger  $m_\chi$ , the cross section also becomes larger. For light DM,  $m_\chi \ll m_e$ , (2) indicates that  $\sigma_{\chi e}^P v_\chi$  for pseudo-scalar type scales as  $m_\chi^4$  while the others as  $m_\chi^2$ . The curves for free electron scattering are fully consistent with the expected scaling behaviors. Including atomic effects would reduce the total cross section due to binding energy of the initial electron. For inner shells, such as  $E_b = (4.53, 0.95)$  keV for  $(2p, 3p)$  electrons, the binding energy can be as large as the recoil energy  $T_r$  to significantly reduce the event rate. The green lines show the ratio between the total cross sections with bound and free electrons. A reduction of  $0.5 \sim 0.7$  can happen. With smaller  $m_\chi$ , the energy release is also smaller and consequently harder to overcome the atomic bound energy which leads to a larger suppression in the total cross section.

### B. Confronting the Xenon1T and PandaX-II Data

In 2020, both Xenon1T and PandaX-II collaborations published their electron recoil spectrum [106, 112]. An excess around  $(2 \sim 3)$  keV appears in the Xenon1T data with significance reaching  $3\sigma$ . This could be explained by the  $\beta$  decays of tritium at  $3.2\sigma$  with a concentration in xenon of  $(6.2 \pm 2.0) \times 10^{-25}$  mol/mol, but “*such a trace amount can neither be confirmed nor excluded*” [106]. The PandaX-II data is fully consistent with such a founding [112]. Since a sub-MeV fermionic DM absorption also leaves a sharp peak at low recoil energy as shown in Fig. 1, confronting the the Xenon1T and PandaX-II data can also provide a meaningful constraint on the preferred parameter space.

The event rate of DM direct detection,

$$\frac{dN}{dT_r} = N_T \frac{\rho_\chi}{m_\chi} t \times \epsilon(T_r) \frac{d\langle\sigma_{\chi e} v_\chi\rangle}{dT_r}, \quad (7)$$

scales with for the number of Xenon atoms  $N_T$ , DM local number density  $\rho_\chi/m_\chi$ , and run time  $t$ . The Xenon1T analysis uses 0.65 tonne-years of data and PandaX-II 100 has tonne-days. In addition, the detection efficiencies are basically constant above  $(3 \sim 4)$  keV and decreases to 0 below there [106].

We adopt the analytical  $\chi^2$  analysis [113, 114], whose advanced version is summarized in App. A, to estimate the sensitivity. In addition to the fermionic DM absorption signal, background estimations are taken from the experimental papers [106]. The results are shown in Fig. 2 for the fit with Xenon1T (left panel) and PandaX-II (right panel) data. Since the different DM absorption operators share roughly the same spectrum shape, one representative vector case can already show the features clearly. For Xenon1T, the best fit is at  $m_\chi = 59$  keV and  $\Lambda = 1$  TeV, being consistent with [105]. The inset plot shows the signal and background curves with the best fit values. The fermionic DM absorption signal with peak at  $T_r = 3.1$  keV can fit the Xenon1T excess very nicely. Comparing with the background-only fit, the  $\chi_{\min}^2$  decreases from 46.3 to 32.2. The decreasing edge for  $m_\chi \rightarrow 20$  keV is due to two major reasons: 1) the cross section decreases with  $m_\chi^2$  in this region and 2) the

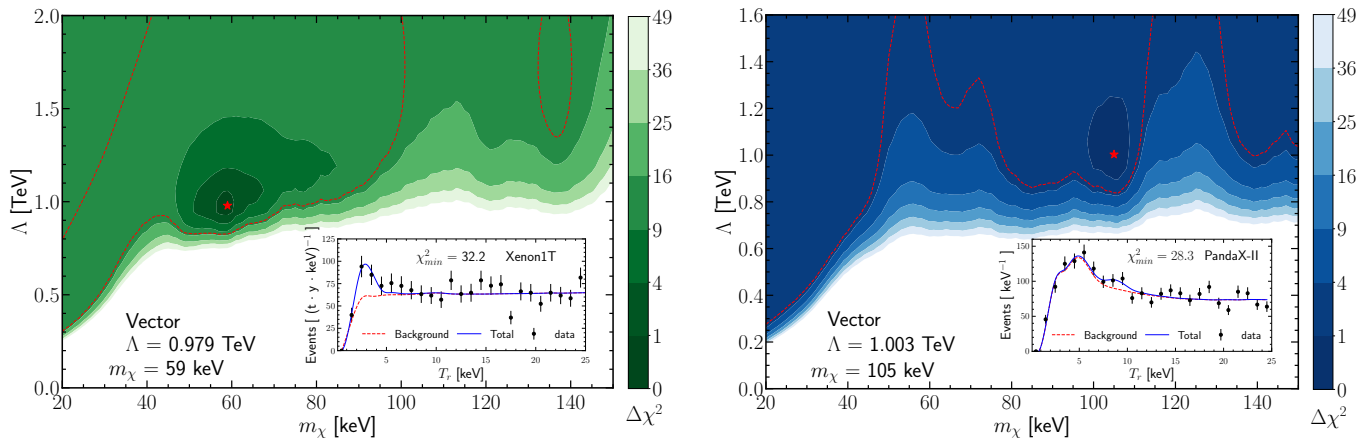


FIG. 2. The best fits (red star) and sensitivity contours of fermionic DM absorption at Xenon1T (**Left**) and PandaX-II (**Right**). Deeper color corresponds to smaller  $\Delta\chi^2$  and the white region has been excluded with  $\Delta\chi^2 > 49$ . For illustration, only the vector case is shown with best fit values  $m_\chi = 59$  keV and  $\Lambda = 0.979$  TeV at Xenon1T while  $m_\chi = 105$  keV and  $\Lambda = 1.003$  TeV at PandaX-II. The red dashed contour shows the 95% C.L. for comparison with other plots. In addition to data points (black), the inset plots demonstrate the background (red dashed) and total (blue solid) event rates with the corresponding best fit values.

efficiency further suppresses its event rate to make it less sensitive. Both needs compensation of a larger coupling strength, or equivalently a lower cut-off scale  $\Lambda$ . On the other side, the rising edge for  $m_\chi \rightarrow 150$  keV at Xenon1T is due to the abnormally lower data point around (17 ~ 18) keV where the recoil spectrum peaks. For PandaX-II data [112], the best fit is at  $m_\chi = 105$  keV corresponding to the small excess at  $T_r = (8 \sim 9)$  keV. Since the peak is not that significant, the  $\chi^2_{\min}$  decreases by only less than 3 from 31.0 of the background-only fit to 28.3. Different from the Xenon1T data, the  $T_r = (17 \sim 19)$  keV data points are higher than the expected background instead which leads to a flat tail for  $m_\chi \rightarrow 150$  keV.

### III. THE DM OVERPRODUCTION IN THE EARLY UNIVERSE

A light DM is typically produced non-thermally. This is because the thermal freeze-out give a relic density  $\rho_\chi \propto m_\chi^2 / \langle \sigma v \rangle$  as ratio between the DM mass and the thermally averaged cross section [115]. To obtain the correct relic density, the interaction strength between DM and SM particles should scale linearly with its mass. Consequently, a light DM typically has a very small coupling with SM particles. Then it is difficult for the light DM to reach thermal equilibrium with the environmental plasma before the thermal freeze-out [116]. Their production is usually realized by the so-called freeze-in mechanism [117–121]. No matter how the DM relic density is generated, it cannot exceed the observed value,  $\Omega_{\text{dm}} h^2 \approx 0.12$  [122].

#### A. Boltzmann Equation and Its Solution

For the fermionic DM absorption on electron target, it is intrinsically connected to electron and positron as demonstrated by the operators in (1). The light DM can be produced by the pair annihilation process  $e^+e^- \rightarrow \chi\nu$ . The Boltzmann equation governing the evolution of DM number density  $n_\chi$  is,

$$\frac{dn_\chi}{dt} + 3Hn_\chi = \int d\Pi_\chi d\Pi_\nu d\Pi_{e^-} d\Pi_{e^+} (2\pi)^4 \delta^{(4)}(p_{e^+} + p_{e^-} - p_\chi - p_\nu)$$

$$\times [|\mathcal{M}|_{e^+e^- \rightarrow \nu\chi}^2 f_{e^+} f_{e^-} (1 - f_\nu)(1 - f_\chi) - |\mathcal{M}|_{\nu\chi \rightarrow e^+e^-}^2 f_\nu f_\chi (1 - f_{e^+})(1 - f_{e^-})], \quad (8)$$

where  $H$  is the Hubble parameter. For particle  $i$ ,  $f_i$  is its phase space distribution function and  $d\Pi_i \equiv d^3p_i/2E_i(2\pi)^3$  is the phase space integration element.

With the freeze-in mechanism, the DM density increases from 0. During the production process,  $f_\chi \ll f_{e^+}, f_{e^-}$ . For simplicity, the second term of (8) can be omitted [121] and the Boltzmann equation then reduces to,

$$\frac{dn_\chi}{dt} + 3Hn_\chi = \langle v_{\text{Mø}} \sigma_{e^+e^-} \rangle n_{e^+}^{\text{eq}} n_{e^-}^{\text{eq}}, \quad (9)$$

where  $v_{\text{Mø}}$  is the Møller velocity of incoming electron/positron pair [123] and  $n_{e^\pm}^{\text{eq}}$  are their number density at thermal equilibrium. We will come back to provide a detailed justification of this simplification later.

To solve the Boltzmann equation, we introduce the DM yield  $Y \equiv n_\chi/s(T)$  as the ratio of DM number density  $n_\chi$  over the entropy density  $s(T)$  as a function of temperature  $T$ . At the epoch of DM production, the universe is dominated by radiation. Both the Hubble parameter  $H$  and entropy density  $s(T)$  can evolve with temperature,

$$H = 1.66\sqrt{g_*} \frac{T^2}{M_P}, \quad s(T) = g_{*s} \frac{2\pi^2}{45} T^3, \quad (10)$$

where  $M_P = 1.22 \times 10^{19}$  GeV is the Planck mass. The relativistic degrees of freedom  $g_* = g_*(T)$  and  $g_{*s} = g_{*s}(T)$  associated with the energy and entropy densities, respectively, are taken from [124] while more detailed discussions can be found in [125, 126]. Although the DM yield keeps increasing, the effective degrees of freedom are mainly contributed by the SM particles. Then in terms of yield  $Y$ , the Boltzmann equation (9) becomes,

$$\frac{dY}{dT} = -\frac{45M_P}{2\pi^2(1.66\sqrt{g_*})\tilde{g}_{*s}T^6} \langle v_{\text{Mø}} \sigma_{e^+e^-} \rangle n_{e^+}^{\text{eq}} n_{e^-}^{\text{eq}}, \quad \text{with} \quad \tilde{g}_{*s} \equiv g_{*s} \left(1 + \frac{T}{3g_{*s}} \frac{dg_{*s}}{dT}\right)^{-1}. \quad (11)$$

The minus sign in  $dY/dT$  arises because the temperature decreases with time but the DM yield  $Y$  increases.

The electron and positron annihilation  $e^+e^- \rightarrow \chi\nu$  happens when the temperature decreases to around the electron mass,  $T \sim 2m_e$  [127]. Then the inverse process  $\chi\nu \rightarrow e^+e^-$  starts to decrease and the  $e^\pm$  density becomes exponentially suppressed. In other words, the Fermi-Dirac distribution of electron (positron) can be approximated by the Maxwell-Boltzmann distribution  $f_{e^\pm}^{\text{eq}} \approx e^{-E/T}$ . For quantitative illustration, the typical electron (positron) energy is  $E_e \approx 2.27$  MeV at  $T \approx 1$  MeV to  $E_e \approx 1.01$  MeV at  $T \approx 0.4$  MeV. Correspondingly, the Maxwell-Boltzmann distribution gives  $e^{-E/T} = 0.104$  at  $T \approx 1$  MeV and 0.080 at  $T \approx 0.4$  MeV, which are very close to the Fermi-Dirac values 0.094 and 0.074, respectively. This further simplifies the thermally averaged cross section  $\langle v_{\text{Mø}} \sigma_{e^+e^-} \rangle$  [123],

$$\langle v_{\text{Mø}} \sigma_{e^+e^-} \rangle n_{e^+}^{\text{eq}} n_{e^-}^{\text{eq}} = \frac{T}{8\pi^4} \int_{4m_e^2}^{\infty} ds (s - 4m_e^2) \sqrt{s} K_1 \left( \frac{\sqrt{s}}{T} \right) \sigma_{e^+e^-}(s), \quad (12)$$

where  $K_1$  is the first modified Bessel function of second kind and  $s \equiv (p_{e^-} + p_{e^+})^2$  is the electron positron invariant mass squared.

The solution of the Boltzmann equation in (11) can be obtained by integrating the temperature  $T$  from neutrino decoupling  $T_{\text{max}} \approx 1$  MeV,

$$Y(T) = \frac{45M_P}{16\pi^6} \int_T^{T_{\text{max}}} \frac{d\tilde{T}}{(1.66\sqrt{g_*})\tilde{g}_{*s}\tilde{T}^5} \int_{4m_e^2}^{\infty} ds (s - 4m_e^2) \sqrt{s} K_1 \left( \frac{\sqrt{s}}{\tilde{T}} \right) \sigma_{e^+e^-}(s). \quad (13)$$



For the DM absorption operators in (1), the  $e^-e^+ \rightarrow \nu\chi$  cross section is a function of the invariant mass  $s$ ,

$$\sigma_{e^+e^-}^S = \frac{1}{\Lambda^4} \frac{\sqrt{s - 4m_e^2}(s - m_\chi^2)^2}{32\pi s \sqrt{s}}, \quad (14a)$$

$$\sigma_{e^+e^-}^P = \frac{1}{\Lambda^4} \frac{(s - m_\chi^2)^2}{32\pi \sqrt{s} \sqrt{s - 4m_e^2}}, \quad (14b)$$

$$\sigma_{e^+e^-}^V = \frac{1}{\Lambda^4} \frac{(s + 2m_e^2)(2s + m_\chi^2)(s - m_\chi^2)^2}{48\pi s^2 \sqrt{s} \sqrt{s - 4m_e^2}}, \quad (14c)$$

$$\sigma_{e^+e^-}^A = \frac{1}{\Lambda^4} \frac{[2s(s - 4m_e^2) + m_\chi^2(s + 2m_e^2)](s - m_\chi^2)^2}{48\pi s^2 \sqrt{s} \sqrt{s - 4m_e^2}}, \quad (14d)$$

$$\sigma_{e^+e^-}^T = \frac{1}{\Lambda^4} \frac{(s + 2m_e^2)(s + 2m_\chi^2)(s - m_\chi^2)^2}{12\pi s^2 \sqrt{s} \sqrt{s - 4m_e^2}}. \quad (14e)$$

Fig. 3 shows the evolution of the DM yield  $Y(T)$  as a function of temperature  $T$ . For illustration, we adopt the scale  $\Lambda = 1$  TeV and DM mass  $m_\chi = 60$  keV. For all the five DM absorption operators, the DM yield converges when the Universe cools down to  $T \sim 0.4$  MeV. In the light DM limit,  $m_\chi \ll m_e \lesssim \sqrt{s}$ , the cross sections in (14) have quite simple scaling behaviors,  $\sigma_{e^+e^-}^{S,P,V,A,T} \approx (\frac{1}{8}, \frac{1}{8}, \frac{1}{6}, \frac{1}{6}, \frac{1}{3}) \times s/4\pi\Lambda^4$ . There is no big difference among scalar and pseudo-scalar operators or among the vector and axial vector ones as correctly reflected in Fig. 3. With larger cross section, the DM yield converges to a larger value. Between the scalar/pseudoscalar group and the vector/axial vector group, the converging values of the DM yield roughly differs by a factor of 3/4 which is consistent with the relative size among the cross sections,  $\sigma_{e^+e^-}^{S,P}/\sigma_{e^+e^-}^{V,A} \approx 3/4$ . The small deviation comes from the finite size of the DM mass  $m_\chi = 60$  keV that is used in Fig. 14. The DM yield scales linearly with the  $e^+e^- \rightarrow \chi\nu$  cross section. We can also check that between the vector/axial vector group and the tensor operator, the factor of 2 difference is also consistent with both sides.

### B. Consistency Check of the Simplified Boltzmann Equation

Before proceeding to constrain the coupling strength of the DM absorption operators, we need to first justify the omission of the second term in (8) for consistency check. The freeze-in production of DM spans from neutrino decoupling ( $T \sim 1$  MeV) to the end of  $e^+e^-$  annihilation ( $T \sim 0.1$  MeV) [127]. During this period of time, electrons and positrons are still in equilibrium with the thermal bath and therefore follow the Fermi-Dirac distribution,  $f_{e^\pm} \equiv 1/(e^{E_{e^\pm}/T} + 1)$ . The most likely value of the electron/positron energy maximizes the energy distribution  $\sqrt{E_e^2 - m_e^2} E_e f_e^{\text{eq}}$ . For example, the peak energy is  $E_e \approx 2.27$  MeV at  $T \approx 1$  MeV and  $E_e \approx 1.01$  MeV at  $T \approx 0.4$  MeV. Correspondingly, the phase space distribution function is roughly  $f_e^{\text{eq}} \sim 0.094$  (0.074) at  $T \approx 1$  MeV (0.4 MeV). Therefore, we can approximate  $(1 - f_{e^\pm}) \approx 1$  in the second term of (8).

The cosmological evolution of DM density is related to the observed number density  $n_\chi^0 = \rho_\chi/m_\chi$  today. Especially, the maximal value of  $n_\chi$  at the end of freeze-in process is  $n_\chi^0/a^3$  neglecting the possible DM decay. At temperature  $T = 0.4$  MeV, the scale factor  $a \equiv 1/(1+z)$  or equivalently the redshift is  $z \approx 1/a \approx 1.6 \times 10^9$  [1]. The upper limit is reached when the freeze-in process contributes the full DM density. Since the DM is not in thermal equilibrium, one can only use the typical energy

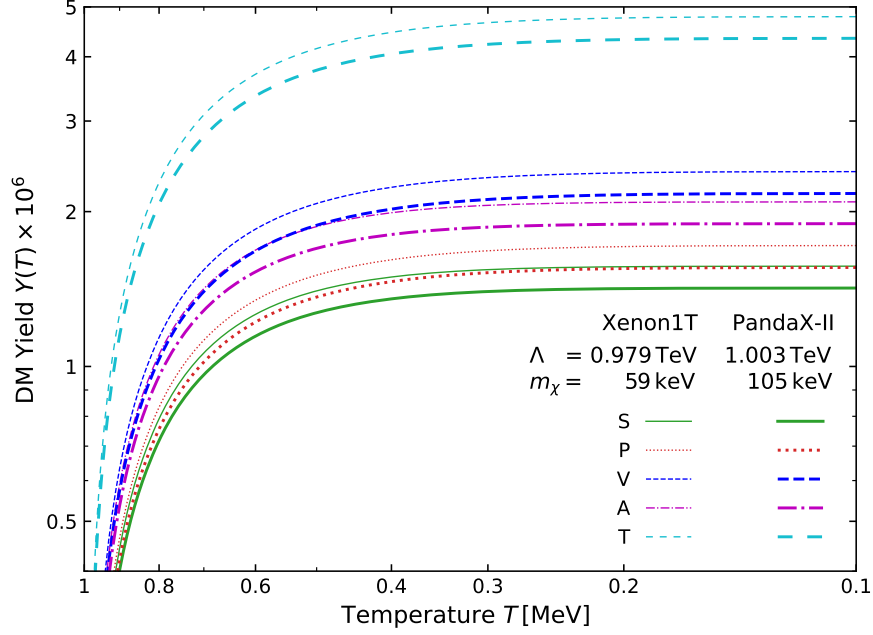


FIG. 3. The evolution of the DM yield  $Y(T)$  as function of temperature  $T$  for the DM absorption operators with the best fit values  $m_\chi = 59$  (105) keV and  $\Lambda = 0.979$  (1.003) TeV of the Xenon1T (PandaX-II) data as shown in thin (thick) lines. The different fermionic DM absorption operators are shown with different line types and colors: scalar (S: green solid), pseudo-scalar (P: red dotted), vector (V: blue dashed), axial vector (A: purple dash-dotted), and tensor (T: cyan long dashed).

$\bar{E}_\chi$  to estimate the size of the phase space distribution function,

$$n_\chi = \int \frac{d^3p}{(2\pi)^3} f_\chi \approx \frac{1}{2\pi^2} f_\chi(\bar{E}_\chi) \bar{E}_\chi^3 \lesssim \frac{n_\chi^0}{a^3} \approx \frac{\rho_\chi^0}{m_\chi} z^3 \approx 4 \times 10^{-5} \text{ MeV}^3 \frac{\text{keV}}{m_\chi}. \quad (15)$$

The typical DM energy can be determined using the energy conservation condition  $E_\chi + E_\nu = E_{e^+} + E_{e^-}$  with the typical electron and positron energies  $E_{e^\pm}$ . In a head-on collision and  $E_{e^+} = E_{e^-}$ , the neutrino energy  $E_\nu = \sqrt{E_\chi^2 - m_\chi^2}$  is directly related to the DM momentum and the DM energy is solved to be  $E_\chi = [m_\chi^2 + (E_{e^-} + E_{e^+})^2]/[2(E_{e^-} + E_{e^+})]$ . For a sub-MeV DM with  $m_\chi \ll E_{e^\pm}$ , the DM energy has a lower limit,  $E_\chi \gtrsim (E_{e^-} + E_{e^+})/2$  which is approximately 1 MeV at  $T \approx 0.4$  MeV. The typical DM phase space factor is then bounded from above,

$$f_\chi \lesssim 4 \times 10^{-5} \text{ MeV}^3 \frac{\text{keV}}{m_\chi} \frac{2\pi^2}{\bar{E}_\chi^3} \approx 8 \times 10^{-4} \frac{\text{keV}}{m_\chi}, \quad (16)$$

which is truly small comparing the electron counterpart,  $f_e \sim 0.1$ .

For the neutrino phase space distribution  $f_\nu$ , there are two components. One is the standard cosmic neutrino background that was in thermal equilibrium and follows the Fermi-Dirac distribution  $f_\nu^{\text{eq}} \equiv 1/(e^{E_\nu/T} + 1)$ . The other one is the associated production from  $e^+e^- \rightarrow \chi\nu$  that shares a similar contribution ( $f_\nu \lesssim 10^{-3}$ ) as DM. So we can approximate  $f_\nu \approx f_\nu^{\text{eq}}$ . Based on a similar analysis as for  $f_e^{\text{eq}}$  by requiring that  $E_\nu^2 f_\nu^{\text{eq}}$  takes its maximal value, one can obtain the typical neutrino energy  $E_\nu \approx 2.22$  (0.89) MeV at  $T \approx 1$  (0.4) MeV. This further leads to a typical phase space distribution  $f_\nu^{\text{eq}} \approx 0.1$ . With massless neutrino, this estimation is independent of  $T$  since its phase space distribution function only depends on the ratio  $E_\nu/T$ . Therefore, we also approximate  $1 - f_\nu \approx 1$  to very good accuracy.

Putting things ( $f_{e^\pm}$ ,  $f_\chi$ , and  $f_\nu$ ) together, we can justify the simplification of omitting the second term in (8). At the converging point ( $T \approx 0.4$  MeV) of DM yield, the phase space factor ratio

$$\frac{f_{e^+}f_{e^-}}{f_\nu f_\chi} \gtrsim 61 \frac{m_\chi}{\text{keV}} \gg 1, \quad (17)$$

for the sub-MeV DM  $1 \text{ keV} \lesssim m_\chi \lesssim 1 \text{ MeV}$  clearly indicates that the first term of (8) dominates over the second one [121].

### C. Constraints from DM Overproduction

To estimate the DM yield today  $Y_0$ , we assume there is no other mechanisms to produce/deplete DM after its production after the converging point  $T_{\min}$ . Then  $Y_0 = Y(T_{\min})$  with time-independence since both the DM number density  $n_\chi$  and the entropy density  $s$  scales as  $1/a^3$ . The DM relic density is estimated as,

$$\Omega_\chi h^2 = \frac{2m_\chi Y_0 s_0 h^2}{\rho_c}, \quad (18)$$

where  $s_0 = 2970 \text{ cm}^{-3}$  is the present entropy density and  $\rho_c = 1.054 \times 10^{-5} h^2 \text{ GeV cm}^{-3}$  the critical density. The Hubble constant  $h = 0.67$  is in unit of  $100 \text{ km s}^{-1} \text{ Mpc}^{-1}$ . Since both DM and its anti-particle can be produced, there is a factor of 2 in the above estimation. Requiring the DM relic density to be less than the measured value,  $\Omega_\chi h^2 \lesssim 0.12$ , sets a lower bound on the new physics scale  $\Lambda$  of the DM absorption operators in (1). In other words, the DM relic density cannot be overproduced.

Fig. 4 shows the constraints on the direct detection cross section  $\sigma_{\chi e} v_\chi$ . The excluded parameter space by the DM overproduction is shown as filled region with dashed boundary. These DM overproduction bounds are quite stringent in the low mass region, especially for the pseudo-scalar case. This is because for  $m_\chi \ll 2m_e$ , the cross-section scales as  $\sigma_{e^-e^+} \propto 1/\Lambda^4$  and becomes independent of the DM mass according to (14). Consequently, the DM yield  $Y$  estimated by (13) is not sensitive to  $m_\chi$  and the DM relic density scales as  $\Omega_\chi h^2 \propto m_\chi/\Lambda^4$ . However, the direct detection cross section in (2) scales as power of the DM mass,  $\sigma_{\chi e}^P v_\chi \propto m_\chi^4/\Lambda^4 \propto m_\chi^3 \Omega_\chi$  for the pseudo-scalar case and  $\sigma_{\chi e}^{V,S,A,T} v_\chi \propto m_\chi^2/\Lambda^4 \propto m_\chi \Omega_\chi$  for the others. This explains why the pseudo-scalar bound decreases faster with  $m_\chi$ . For the scalar, (axial-)vector, and tensor cases, they have a similar sensitivity around  $10^{-50} \text{ cm}^2$  to  $10^{-47} \text{ cm}^2$  for the DM mass from 1 keV to 1 MeV.

Using the more exactly calculated cross section  $\sigma_{\chi e} v_\chi$  as summarized in (2), instead of the approximation  $m_\chi^2/4\pi\Lambda^4$  in the  $m_\chi \ll m_e$  limit, for the vertical axis has some advantage. As explained below (14), the  $e^+e^- \rightarrow \chi\nu$  cross section almost degenerates between scalar ( $\sigma_{e^+e^-}^S$ ) and pseudo-scalar ( $\sigma_{e^+e^-}^P$ ) operators. So one may expect their overproduction limits not to differ much and hard to distinguish in Fig. 4 is the universal  $m_\chi^2/4\pi\Lambda^4$  is adopted. In contrast, the direct detection cross sections  $\sigma_{\chi e}^S v_\chi$  and  $\sigma_{\chi e}^P v_\chi$  have quite different scaling behaviors as discussed around (2). So we can still see the clear difference between the scalar and pseudo-scalar cases in Fig. 4. In addition,  $\sigma_{\chi e}$  also has the advantage of being able to reflect the realistic direct detection signal strength.

For comparison, the best fit points (star) with the Xenon1T (light green) and PandaX-II (yellow) are also shown. The best fit values are taken from Fig. 2 for the vector case. We can see that for both data sets, the best fit points are already at the boundary of the DM overproduction constraints. Also shown are the 95% C.L. allowed regions for the Xenon1T (light green contour) and PandaX-II (yellow contour) data. Consistent with the 95% C.L. contours in Fig. 2, the 95% C.L. allowed parameter space here is divided into 2 (3) regions for the Xenon1T (PandaX-II) data. The regions

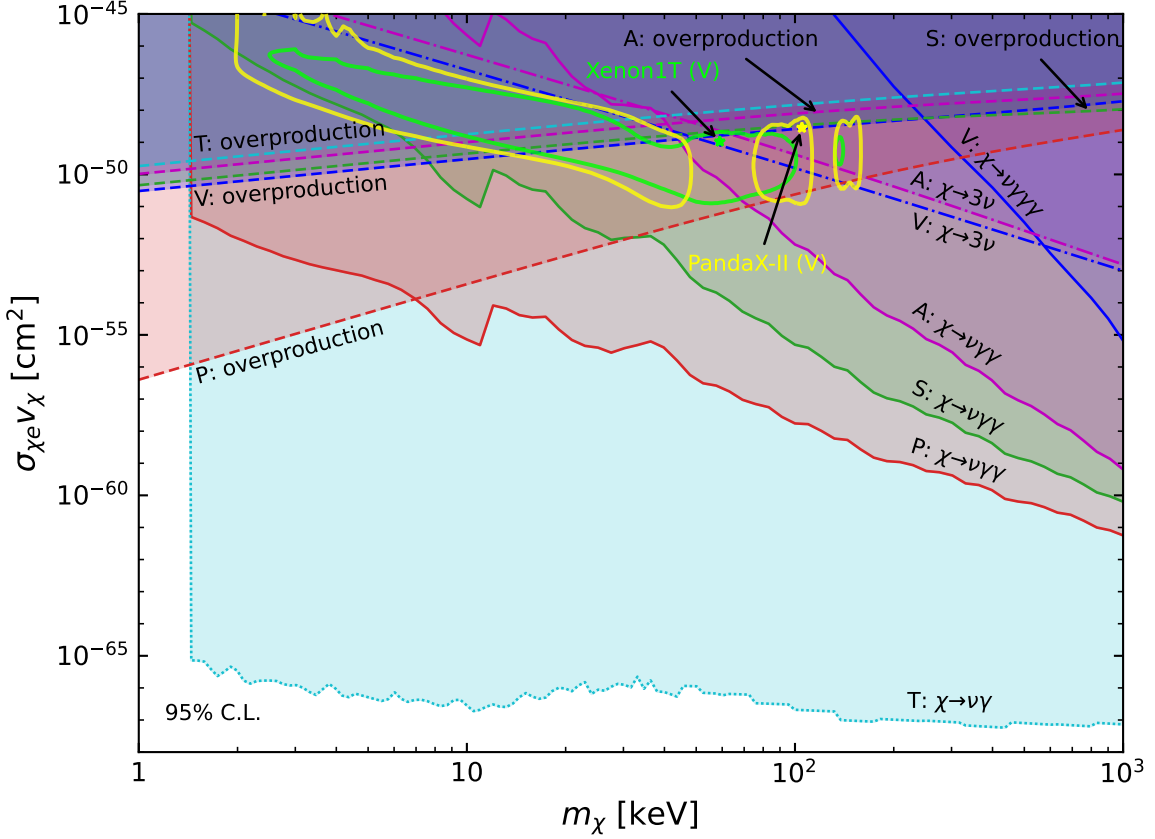


FIG. 4. The 95% C.L. constraints on the fermionic absorption operators from the DM overproduction (filled regions with dashed boundary), the cosmological evolution history (filled regions for invisible decay  $\chi \rightarrow 3\nu$  with dot-dashed boundary), as well as the astrophysical X(gamma)-ray data (filled regions for visible decays  $\chi \rightarrow \nu\gamma(s)$ ). The exclusion regions are filled with colors for scalar (S: green), pseudo-scalar (P: red), vector (V: blue), axial vector (A: magenta), and tensor (T: cyan) operators, respectively. Note that the exclusion region for the tensor operator from astrophysical X(gamma)-ray constraint (T:  $\chi \rightarrow \nu\gamma$ ) uses dotted boundary to indicate that this constraint is subject to uncertainty in the regularization scheme. For comparison, the best fit points (star) and 95% C.L. contours (contour) for the Xenon1T (light green) and PandaX-II (yellow) are also shown with the vector-type operator as an example.

extend significantly down to a few keV of the DM mass  $m_\chi$ . More discussions about the cosmological constraint from the Universe expansion history and the astrophysical ones from various X(gamma)-ray observations will be discussed later in Sec. V A and Sec. V B, respectively.

#### IV. DM DECAY

One important feature of the DM absorption process is that only one DM particle can appear in the process as demonstrated by the general fermionic DM absorption operators in (1). A natural consequence is that DM is unstable and can decay into light SM particles unless forbidden by kinematics. Since the DM particle is neutral, electron and positron should appear as a pair if such decay topology is possible. For  $\chi \rightarrow e^+e^- + \dots$  to happen, the DM mass has to be larger than twice of the electron mass,  $m_\chi > 2m_e$ , which is already outside the mass range considered in the current paper. The only possible decay products are the neutrinos and photons.

With the DM particle being a fermion, the final state has to contain an odd number of neutrinos, including the visible decay modes ( $\chi \rightarrow \nu + \gamma$ ,  $\chi \rightarrow \nu + \gamma\gamma$ , and  $\chi \rightarrow \nu + \gamma\gamma\gamma$ ) as well as the invisible

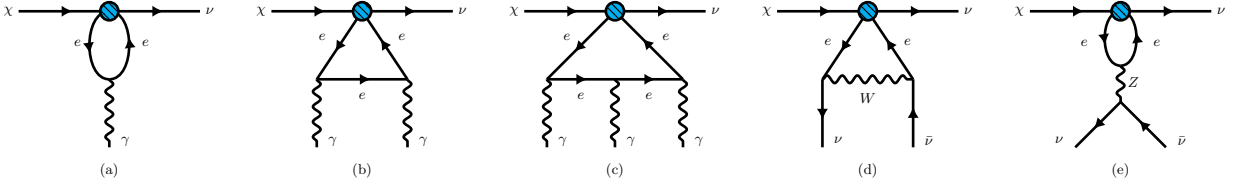


FIG. 5. The representative Feynman diagrams contributing to the DM visible decays  $\chi \rightarrow \nu + \gamma(s)$  as well as the invisible decay  $\chi \rightarrow 3\nu$ . The blue vertex is the DM absorption operator while the others are SM interactions.

mode  $\chi \rightarrow 3\nu$ . All these can happen only at loop level since the absorption operators in (1) contains two electron fields. The leading 1-loop Feynman diagrams are listed in Fig. 5. For the visible decay modes, only electromagnetic interaction of the SM is needed in addition to the absorption operator. In contrast, the invisible decay mode  $\chi \rightarrow 3\nu$  requires the SM weak interactions with  $W/Z$  mediator.

To have a better understanding of the connection between operators and decay processes, Tab. I summarizes the leading decay channels for each operator highlighted with a checkmark ( $\checkmark$ ). The cross ( $\times$ ) indicates the decay channel that cannot be generated at 1-loop level. Although some can appear at two-loop level, they are hugely suppressed by loop factor, the weak scale, and/or phase space. For the  $\chi \rightarrow \nu\gamma\gamma\gamma$  and  $\chi \rightarrow 3\nu$  channels from the tensor operator, the  $\times!$  symbol is used to indicate that such processes can be generated at 1-loop order but heavily suppressed. In the following subsections we detail our calculation for each operator. The calculated decay width and spectrum are further used in Sec. V to derive the cosmological and astrophysical constraints.

Operator \ Process	Process			
	$\chi \rightarrow \nu\gamma$	$\chi \rightarrow \nu\gamma\gamma$	$\chi \rightarrow \nu\gamma\gamma\gamma$	$\chi \rightarrow 3\nu$
S: $\mathcal{O}_{e\nu\chi}^S$	$\times$	$\checkmark$	$\times$	$\times$
P: $\mathcal{O}_{e\nu\chi}^P$	$\times$	$\checkmark$	$\times$	$\times$
V: $\mathcal{O}_{e\nu\chi}^V$	$\times$	$\times$	$\checkmark$	$\checkmark$
A: $\mathcal{O}_{e\nu\chi}^A$	$\times$	$\checkmark$	$\times$	$\checkmark$
T: $\mathcal{O}_{e\nu\chi}^T$	$\checkmark$	$\times$	$\times!$	$\times!$

TABLE I. Contributions of the Fermionic DM absorption operators to the visible ( $\chi \rightarrow \nu\gamma(s)$ ) and invisible ( $\chi \rightarrow 3\nu$ ) decay channels. The one allowed at one-loop level is shown with a checkmark ( $\checkmark$ ) or a cross ( $\times$ ) if otherwise. For those that allowed at one-loop level but highly suppressed, an exclamed cross ( $\times!$ ) is used.

### 1. The Scalar and Pseudoscalar Operators $\mathcal{O}_{e\nu\chi}^{S(P)}$

For the operators  $\mathcal{O}_{e\nu\chi}^{S,P}$  with an electron scalar or pseudo-scalar current, the dominant decay mode is  $\chi \rightarrow \nu + \gamma\gamma$ . As shown in Fig. 5(b), this process is generated through electron loop with two photons attached to the electron loop. The amplitudes from loop calculation are free from the UV divergence. Consequently, the decay widths can be calculated exactly,

$$\Gamma_{\chi \rightarrow \nu\gamma\gamma}^S = \frac{1}{\Lambda^4} \frac{\alpha^2}{2048\pi^5 m_e^2 m_\chi^3} \int_0^{m_\chi^2} ds_{12} s_{12}^2 (m_\chi^2 - s_{12})^2 |F_S(\eta)|^2, \quad (19a)$$

$$\Gamma_{\chi \rightarrow \nu\gamma\gamma}^P = \frac{1}{\Lambda^4} \frac{\alpha^2}{2048\pi^5 m_e^2 m_\chi^3} \int_0^{m_\chi^2} ds_{12} s_{12}^2 (m_\chi^2 - s_{12})^2 |F_P(\eta)|^2, \quad (19b)$$

where  $\alpha \equiv e^4/4\pi$  is the electromagnetic fine structure constant. The integration variable  $s_{12}$  is the squared invariant mass of the two final-state photons, starting from 0 to the maximal value  $m_\chi^2$ . The

loop functions  $F_{S,P}(\eta)$  with  $\eta \equiv s_{12}/m_e^2$  are,

$$F_S(\eta) \equiv \frac{4}{\eta} - \frac{\eta - 4}{\eta^2} \ln^2 \frac{\sqrt{\eta - 4} - \sqrt{\eta}}{\sqrt{\eta - 4} + \sqrt{\eta}}, \quad (20a)$$

$$F_P(\eta) \equiv -\frac{1}{\eta} \ln^2 \frac{\sqrt{\eta - 4} - \sqrt{\eta}}{\sqrt{\eta - 4} + \sqrt{\eta}}. \quad (20b)$$

In the limit of  $m_\chi \ll 2m_e$  and consequently  $s_{12} \ll m_e^2$ , the loop functions reduce to  $F_S(\eta) \approx 2/3$  and  $F_P(\eta) \approx 1$ . Then the decay widths above can be approximated as,

$$\Gamma_{\chi \rightarrow \nu \gamma \gamma}^S \approx 9.4 \times 10^{-20} \text{sec}^{-1} \left( \frac{m_\chi}{200 \text{ keV}} \right)^7 \left( \frac{\text{TeV}}{\Lambda} \right)^4, \quad (21a)$$

$$\Gamma_{\chi \rightarrow \nu \gamma \gamma}^P \approx 2.1 \times 10^{-19} \text{sec}^{-1} \left( \frac{m_\chi}{200 \text{ keV}} \right)^7 \left( \frac{\text{TeV}}{\Lambda} \right)^4. \quad (21b)$$

For the 2-body mode  $\chi \rightarrow \nu \gamma$  in Fig. 5(a) and the 4-body one  $\chi \rightarrow \nu \gamma \gamma \gamma$  in Fig. 5(c), the electron loop contribution vanishes due to the QED (quantum electrodynamics) charge conjugation symmetry. This is because the involved electron currents  $\bar{e}e$  and  $\bar{e}\gamma_5 e$  have an even parity under charge conjugation transformation while the photon field is odd. With an odd number of photons, the one-loop diagram is odd and should vanish. Non-vanishing contribution can only be generated at the 2-loop level involving both QED and weak interactions. However, such a contribution is severely suppressed by the loop factor and weak scale such as  $m_e^2/m_W^2$ . Therefore, we can neglect the single- and triple-photon contributions.

The 3-body invisible decay  $\chi \rightarrow 3\nu$  in the last two diagrams of Fig. 5 is also vanishing. The connection between the  $\chi\nu$  fermion lines at the top and the other two neutrinos is established through the  $\mathcal{O}_{e\nu\chi}^S$  and  $\mathcal{O}_{e\nu\chi}^P$  operators. Correspondingly, the effective current for the other two neutrinos after loop integration should also be of the same scalar feature as the  $\bar{e}e$  and  $\bar{e}\gamma_5 e$  counterpart in the operator. Since the SM neutrinos are massless and purely left-handed, the only possibility is  $\partial_\mu(\bar{\nu}_L \gamma^\mu \nu_L)$  with Lorentz indices fully contracted. Then, the equation of motion for a massless neutrino renders  $\partial_\mu \gamma^\mu \nu_L$  to vanish. Although constructing a Majorana mass term with only left-handed neutrinos is possible, lepton number is not violated in weak interactions and hence cannot appear without involving other new physics.

## 2. The Vector Operator $\mathcal{O}_{e\nu\chi}^V$

For the vector operator, the 2-body  $\chi \rightarrow \nu \gamma$  and 3-body  $\chi \rightarrow \nu \gamma \gamma$  channels cannot arise at 1-loop level. The vanishing of  $\chi \rightarrow \nu \gamma$  is due to the gauge symmetry. As mentioned in the previous paragraph, the electron current  $\bar{e}\gamma_\mu e$  in the vector operator  $\mathcal{O}_{e\nu\chi}^V$  contributes to the loop mediator and needs to be integrated way with a remaining photon field as external state. This feature is generally parametrized as matrix element  $\langle \gamma(q, \epsilon) | \bar{e}\gamma_\mu e | 0 \rangle$ . In the presence of an external photon, the matrix element is a linear function of its polarization vector  $\epsilon_\mu^*$ . Another quantity that can provide a Lorentz index is the momentum transfer  $q_\mu$ . The full matrix element also contains a piece  $\bar{u}_\nu \gamma^\mu P_L u_\chi$  from the neutrino side,

$$\mathcal{M} \equiv [A(q^2)q_\mu \epsilon_\mu^* \cdot q + B(q^2)\epsilon_\mu^*] (\bar{u}_\nu \gamma^\mu P_L u_\chi) \equiv \epsilon_\mu^* \mathcal{M}^\mu. \quad (22)$$

The coefficients  $A(q^2)$  and  $B(q^2)$  correlate with each other by the QED Ward identity:  $q_\mu \mathcal{M}^\mu = 0$  from replacing the photon polarization vector  $\epsilon_\mu^*$  with its four-momentum  $q_\mu$ . Namely,

$$[A(q^2)q^2 + B(q^2)] q_\mu (\bar{u}_\nu \gamma^\mu P_L u_\chi) = 0. \quad (23)$$

Since  $q^\mu \equiv p_\chi^\mu - p_\nu^\mu$ , the second term  $q_\mu(\bar{u}_\nu \gamma^\mu P_L u_\chi) = \bar{u}_\nu(\not{p}_\chi - \not{p}_\nu)P_L u_\chi = m_\chi \bar{u}_\nu P_R u_\chi \neq 0$  is nonzero. Then the only solution is  $B(q^2) = -A(q^2)q^2$  and the effective current,

$$\langle \gamma(q, \epsilon) | \bar{e} \gamma_\mu e | 0 \rangle = A(q^2)(q^2 \epsilon_\mu^* - q_\mu \epsilon^* \cdot q), \quad (24)$$

vanishes due to the photon on-shell ( $q^2 = 0$ ) and transverse ( $\epsilon^* \cdot q = 0$ ) conditions. For the 2-photon decay  $\chi \rightarrow \nu \gamma \gamma$ , the loop part again contains 3 currents and hence vanishes due to the QED charge conjugation symmetry.

The dominant visible decay channel is the 4-body process  $\chi \rightarrow \nu \gamma \gamma \gamma$  whose matrix element can be generally parametrized as,

$$\mathcal{M}_{\nu \gamma \gamma \gamma} = -\frac{e^3}{16\pi^2 \Lambda^2} (\bar{u}_\nu \gamma_\mu P_L u_\chi) \epsilon_{1\alpha}^* \epsilon_{2\beta}^* \epsilon_{3\rho}^* \Pi^{\mu\alpha\beta\rho}, \quad (25)$$

where  $\epsilon_i^*$  is the polarization vector of the  $i$ -th final-state photon. The tensor  $\Pi^{\mu\alpha\beta\rho}$  is the reduced matrix element from the the electron loop in Fig. 5(c). Correspondingly, the spin averaged squared matrix amplitude becomes,

$$|\overline{\mathcal{M}_{\chi \rightarrow \nu \gamma \gamma \gamma}}|^2 = \frac{16\alpha^3}{\pi \Lambda^4} \left\{ -\frac{1}{4} \text{Tr} [\not{p}_\nu \gamma_\mu \not{p}_\chi \gamma_\nu] \left( \frac{1}{8} \Pi^{\mu\alpha\beta\rho} \right) \left( \frac{1}{8} \Pi^\nu_{\alpha\beta\rho} \right) \right\}. \quad (26)$$

The reduced matrix element  $\Pi^{\mu\alpha\beta\rho}$  is evaluated first analytically by Package-X [128] and then numerically by COLLIER [129]. The decay width is an integral over the 4-body phase space  $d\Phi_4$ ,

$$\Gamma_{\chi \rightarrow \nu \gamma \gamma \gamma}^V = \frac{1}{3!} \frac{1}{2m_\chi} \int d\Phi_4 |\overline{\mathcal{M}_{\chi \rightarrow \nu \gamma \gamma \gamma}}|^2, \quad (27)$$

with the factor  $1/3!$  to avoid phase space overcounting for the 3 identical photons. In the limit of  $m_\chi \ll 2m_e$ , the decay width also has a simple scaling behavior,

$$\Gamma_{\chi \rightarrow \nu \gamma \gamma \gamma}^V \approx 2.6 \times 10^{-29} \text{sec}^{-1} \left( \frac{m_\chi}{200 \text{ keV}} \right)^{13} \left( \frac{\text{TeV}}{\Lambda} \right)^4. \quad (28)$$

For the DM invisible decay  $\chi \rightarrow 3\nu$ , the loop diagrams (d) and (e) in Fig. 5 suffer from UV divergence. To make a reasonable estimation, we use the dimensional regularization (DR) to tackle this issue. For the  $W$ -loop contribution, the amplitude in the unitary gauge is

$$\mathcal{M}_{\chi \rightarrow 3\nu}^W = -\frac{\bar{u}_\nu \gamma^\mu P_L u_\chi}{\Lambda^2} \frac{3g_2^2}{64\pi^2} \left[ 1 + \frac{m_e^2}{m_W^2} \left( \frac{1}{\epsilon} + \frac{11}{6} + \ln \frac{\Lambda^2}{m_W^2} \right) + \dots \right] [\bar{u}_{\nu_e}(p_1) \gamma_\mu P_L v_{\nu_e}(p_2)], \quad (29)$$

where  $g_2$  is the weak coupling constant while  $\mu$  the dimensional regularization scale. The terms in the bracket is from the  $W$ -loop for generating the electron neutrino pair, and  $\dots$  stand for terms suppressed by higher powers of  $q^2/m_W^2$ . Dropping the divergent piece  $1/\epsilon$  altogether with the terms proportional to  $q^2/m_W^2$ , the finite amplitude used in our estimation is,

$$\mathcal{M}_{\chi \rightarrow 3\nu}^W \approx -\frac{1}{\Lambda^2} \frac{3g_2^2}{64\pi^2} (\bar{u}_\nu \gamma^\mu P_L u_\chi) [\bar{u}_{\nu_e}(p_1) \gamma_\mu P_L v_{\nu_e}(p_2)]. \quad (30)$$

The amplitude and decay width depend on the neutrino flavor that appears in the DM absorption operator. For  $(\bar{\nu}_e \gamma^\mu \chi_L)$ , there are two diagrams by exchanging the two electron neutrinos but only a single one for  $(\bar{\nu}_{\mu,\tau} \gamma^\mu \chi_L)$ . Considering this difference, the decay width for muon/tau flavor is,

$$\Gamma_{\chi \rightarrow 3\nu}^V \approx \frac{m_\chi^5}{1536\pi^3} \left( \frac{3g_2^2}{64\pi^2} \right)^2 \frac{1}{\Lambda^4} \approx 3.66 \times 10^{-17} \text{sec}^{-1} \left( \frac{m_\chi}{200 \text{ keV}} \right)^5 \left( \frac{\text{TeV}}{\Lambda} \right)^4, \quad (31)$$

and for the electron neutrino in  $\mathcal{O}_{e\nu\chi}^V$ , there is an additional enhancement factor 2. Note that the  $Z$  boson mediated diagram of Fig. 5(e) is always suppressed by  $1/m_Z^2$  and hence can be neglected.

### 3. The Axial-Vector Operator $\mathcal{O}_{e\nu\chi}^A$

The dominant decay modes for the axial-vector operator  $\mathcal{O}_{e\nu\chi}^A$  are the 3-body decay  $\chi \rightarrow \nu\gamma\gamma$  and  $\chi \rightarrow 3\nu$ . This is because the 2-body mode  $\chi \rightarrow \nu\gamma$  and the 4-body one  $\chi \rightarrow \nu\gamma\gamma\gamma$  with an odd number of photons in the final state are forbidden by the QED charge conjugation symmetry.

First, the 3-body process  $\chi \rightarrow \nu\gamma\gamma$  is generated through the similar electron loop as the scalar and pseudo-scalar cases. The exact decay width is,

$$\Gamma_{\chi \rightarrow \nu\gamma\gamma}^A = \frac{1}{\Lambda^4} \frac{\alpha^2}{512\pi^5 m_e^4 m_\chi} \int_0^{m_\chi^2} ds_{12} s_{12}^2 (m_\chi^2 - s_{12})^2 |F_A(\eta)|^2, \quad (32)$$

where  $s_{12}$  is again the squared invariant mass of the two final-state photons and  $\eta \equiv s_{12}/m_e^2$ . The new loop function  $F_A(\eta)$ ,

$$F_A(\eta) \equiv -\frac{1}{\eta} - \frac{1}{\eta^2} \ln^2 \frac{\sqrt{\eta-4} - \sqrt{\eta}}{\sqrt{\eta-4} + \sqrt{\eta}}, \quad (33)$$

reduces to  $F_A(\eta) \approx 1/12$  in the limit of  $m_\chi \ll 2m_e$ . Accordingly, the decay width scales as

$$\Gamma_{\chi \rightarrow \nu\gamma\gamma}^A \approx 9 \times 10^{-22} \text{sec}^{-1} \left( \frac{m_\chi}{200 \text{ keV}} \right)^9 \left( \frac{\text{TeV}}{\Lambda} \right)^4, \quad (34)$$

for tiny DM mass. Note that the dependence on  $m_\chi$  is higher by 2 powers than that of the scalar and pseudo-scalar cases in (21).

Second, the invisible decay  $\chi \rightarrow 3\nu$  shares the similar features as that of the vector case including the divergence. We use the same procedure to keep only the leading non-divergent term,

$$\Gamma_{\chi \rightarrow 3\nu}^A \approx \frac{m_\chi^5}{1536\pi^3} \left( \frac{3g_2^2}{64\pi^2} \right)^2 \frac{1}{\Lambda^4} \approx 3.66 \times 10^{-17} \text{sec}^{-1} \left( \frac{m_\chi}{200 \text{ keV}} \right)^5 \left( \frac{\text{TeV}}{\Lambda} \right)^4. \quad (35)$$

for the  $\mathcal{O}_{e\nu\chi}^A$  operator with a muon/tau neutrino. There is also an additional factor 2 for the electron neutrino case.

### 4. The Tensor Operator $\mathcal{O}_{e\nu\chi}^T$

The dominant decay mode for the tensor operator is the 2-body decay  $\chi \rightarrow \nu\gamma$  in Fig. 5(a). However, it suffers from UV divergence,

$$\mathcal{M}_{\chi \rightarrow \nu\gamma} = \frac{1}{\Lambda^2} (\bar{u}_\nu \sigma^{\mu\nu} P_R u_\chi) \left[ -i \frac{em_e q_\mu \epsilon_\nu^*}{2\pi^2} \left( \frac{1}{\epsilon} + \ln \frac{\Lambda^2}{m_e^2} \right) \right], \quad (36)$$

and needs to be regularized by the DR scheme. The vectors  $q_\mu$  and  $\epsilon_\nu^*$  are the outgoing photon momentum and polarization vector, respectively. After dropping the divergent factor  $1/\epsilon$ , the decay width from the the finite part becomes

$$\Gamma_{\chi \rightarrow \nu\gamma}^T = \frac{\alpha m_e^2 m_\chi^3}{16\pi^4 \Lambda^4} \ln^2 \frac{\Lambda^2}{m_e^2} \approx 1.5 \times 10^{-8} \text{sec}^{-1} \left( \frac{m_\chi}{200 \text{ keV}} \right)^3 \left( \frac{\text{TeV}}{\Lambda} \right)^4 \frac{\ln^2(\Lambda^2/m_e^2)}{1000}, \quad (37)$$

where the cut-off scale  $\Lambda$  enters through the log term. Since the logarithm is not sensitive to the change of  $\Lambda$ , we approximate it by a typical value  $\ln^2(\Lambda^2/m_e^2) \sim \mathcal{O}(10^3)$ . Comparing (37) with (21), (28) and (34), we see that the  $\chi \rightarrow \nu\gamma$  decay width for  $\mathcal{O}_{e\nu\chi}^T$  is much larger than the dominant visible decay width for all other operators. This implies that a much stronger constraint will be put on the



tensor operator. Again, the 3-body channel  $\chi \rightarrow \nu\gamma\gamma$  vanishes due to the QED charge conjugation symmetry. In addition, the 4-body decay  $\chi \rightarrow \nu\gamma\gamma\gamma$  is suppressed by additional couplings as well as phase space factor.

For the invisible decay  $\chi \rightarrow 3\nu$ , as dictated by Lorentz invariance and the left-handedness of SM neutrinos, the electron tensor structure  $(\bar{e}\sigma^{\mu\nu}e)$  induces an effective operator  $(m_e/m_W^2)\partial^\mu(\bar{\nu}_L\gamma^\nu\nu_L)$  after loop integration. The electron mass  $m_e$  comes from the chirality flip introduced by the tensor operator. With the mass dimensions of  $m_e$  and  $\partial^\mu$  compensated by  $1/m_W^2$ , this contribution is severely suppressed by a factor  $m_e^2/m_W^2 \sim 10^{-11}$  than  $\chi \rightarrow \nu\gamma$  and can be safely neglected.

## V. THE COSMOLOGICAL AND ASTROPHYSICAL CONSTRAINTS ON DM DECAYS

As elaborated above, the DM absorption operators contain only one DM field. There is no intrinsic mechanism to forbid DM from decaying. This can provide some visible effect on the cosmological evolution history and the astrophysical observations via X-ray and gamma ray. This section evaluates first the constraints from cosmology in Sec. VA and astrophysical observations in Sec. VB.

### A. The Cosmological Evolution Constraints on the DM Invisible Decay $\chi \rightarrow 3\nu$

As illustrated in Sec. IV, both the vector and axial-vector operators can have invisible decay  $\chi \rightarrow 3\nu$ . More importantly, the invisible decay mode dominates over the visible ones by at least 4 orders. This can be seen by comparing (28) with (31), and (34) with (35). If a significant amount of the DM decays invisibly to inject its energy into relativistic degrees of freedom, the expansion history of the Universe can receive sizable modifications. Previous studies have already put quite strong constraints on the decaying DM scenario [130–133]. The currently most stringent constraint is  $\Gamma_{\text{inv}}^{-1} < 468 \text{ Gyr}$  [134].

The constraints on  $\sigma_{\chi e}^{V,A}v_\chi$  are shown as dot-dashed lines in Fig. 4. The blue one is for the vector case while the magenta one for the axial-vector one. In the mass range  $40 \text{ keV} \lesssim m_\chi \lesssim 500 \text{ keV}$ , the constraints from  $\chi \rightarrow 3\nu$  for the vector case is stronger than the DM overproduction and gamma-ray constraints. Together with the approximation  $\sigma_{\chi e}v_\chi \approx m_\chi^2/4\pi\Lambda^4$ , the scaling behaviors  $\Gamma_{3\nu}^{V,A} \propto m_\chi^5/\Lambda^4$  in (31) and (35) renders the constraint to scale as  $\propto 1/m_\chi^3$ . This estimation is consistent with the resulting curves shown in Fig. 4. For other operators, the  $\chi \rightarrow 3\nu$  channel is much smaller.

### B. The Astrophysical X-Ray and Gamma Ray Constraints on the Visible Decays $\chi \rightarrow \nu + \gamma(s)$

Although the visible decays are typically much smaller than the invisible one as explored in Sec. IV, it is much easier to observe photon than neutrino. This is especially true in the low energy range for sub-MeV DM. With DM distributing everywhere in the Universe and being especially concentrated in our Milky Way galaxy, the observation of diffuse X-ray and gamma ray can put stringent constraints on the decay width and therefore the cut-off scale  $\Lambda$ . We first describe how the DM visible decays contribute to the X(gamma)-ray observations in Sec. VB1 and then compare with the astrophysics observation data sets in Sec. VB2.

1. X-Ray and Gamma Ray Fluxes from the Visible Decays

Both galactic and extra-galactic sources of DM visible decay  $\chi \rightarrow \nu\gamma(s)$  can contribute to the X(gamma)-ray observations around our Earth. Typically the extra-galactic contributions are much smaller than the galactic counterpart. But for those diffuse cosmic fluxes, the major contribution comes from extra-galactic sources. So we will discuss both contributions below.

For DM decay, the galactic contribution is proportional to its local density  $\rho_\chi/m_\chi$  and the decay spectrum  $d\Gamma_\chi/dE_\gamma$  calculated in the rest frame of DM. So the differential photon flux per unit energy per solid angle is,

$$\frac{d^2\Phi_\gamma}{dE_\gamma d\Omega} = \frac{1}{4\pi} \frac{d\Gamma_\chi}{dE_\gamma} \int_{\text{l.o.s.}}^{s_{\max}} \frac{\rho_\chi(r)}{m_\chi} ds, \quad (38)$$

where  $d\Gamma_\chi/dE_\gamma$  is the corresponding differential decay width. The integration over the line of sight (l.o.s.) takes all the contribution along a specific direction. Note that the DM density  $\rho_\chi(r)$  is a direct function of the distance  $r$  from the galactic center. We adopt the NFW profile,  $\rho(r) = \rho_0/[(r/r_s)(1+r/r_s)^2]$  [135, 136], where  $r_s = 17$  kpc [137] and  $\rho_0 = 0.43$  GeV/cm<sup>3</sup> to give the local DM density  $\rho_\chi \approx 0.4$  GeV/cm<sup>3</sup>. The distance  $r(s)$  is a function of the l.o.s. distance  $s$  in the galactic coordinate,

$$r(s) = \sqrt{r_\odot^2 + s^2 - 2r_\odot s \cos\psi}. \quad (39)$$

In addition,  $r_\odot = 8.3$  kpc is the distance of Earth to the galactic center and  $\cos\psi \equiv \cos b \cos l$ . The integration range for the l.o.s. distance  $s$  is from 0 to a maximal value determined by the virial radius  $r_{\text{vir}} = 300$  kpc of the DM halo [9],

$$s_{\max} = r_\odot \cos\psi + \sqrt{r_{\text{vir}}^2 - r_\odot^2 \sin^2\psi}. \quad (40)$$

The extra-galactic contribution comes from the smooth DM distribution in the whole universe. Its contribution is isotropic and integrated over a large range of the redshift [138],

$$\frac{d^2\Phi_r^{\text{EG}}}{dE_\gamma d\Omega} = \frac{\Omega_{\text{DM}}\rho_c}{4\pi m_\chi H_0 \sqrt{\Omega_m}} \int_0^\infty \frac{d\Gamma_\chi}{dE_\gamma(z)} \frac{dz}{\sqrt{\kappa + (1+z)^3}}. \quad (41)$$

The Hubble constant  $H_0 = 67.4$  km sec<sup>-1</sup>Mpc<sup>-1</sup> and the cosmological critical density  $\rho_c = 5.8 \times 10^{-6}$  GeV cm<sup>-3</sup> are present values. Of the total matter fraction  $\Omega_m = 0.315$ , DM takes the largest share  $\Omega_{\text{DM}} = 0.265$ . In addition, the dark energy (DE) also has a large effect on the cosmological evolution, especially in the late stage. We use  $\kappa \equiv \Omega_\Lambda/\Omega_m = 2.17$  to parametrize the contribution of DE. The decay width and spectrum calculated in Sec. IV cannot be used directly. Due to cosmological redshift, the photon energy  $E_\gamma(z) = (1+z)E_\gamma$  emitted at redshift  $z$  is  $1+z$  times of the apparent  $E_\gamma$ .

The total photon flux  $d^2\Phi_\gamma/dE_\gamma d\Omega$  due to DM decay is then a sum of the above two components. For a telescope with effective area  $A_{\text{eff}}$  and field of view (FOV)  $\Delta\Omega$  as well as exposure time  $T_{\text{obs}}$ , the predicted photon event rate in energy bin  $[E_i^-, E_i^+]$  is

$$N_i^{\text{th}} \equiv A_{\text{eff}} T_{\text{obs}} \int_{E_i^-}^{E_i^+} dE_\gamma \int_{\Delta\Omega} d\Omega \frac{d^2\Phi_\gamma}{dE_\gamma d\Omega}. \quad (42)$$

Below we use real data to constrain the DM decay width and subsequently the DM coupling strength.

2. Constraints from Astrophysical X-ray and Gamma Ray Data in the keV-MeV Range

As argued at the beginning of Sec. II, we are interested in the DM mass range between keV and MeV. The relevant observations in our analysis include Insight-HXMT [139], NuSTAR [140, 141], HEAO-1 [142], and INTEGRAL [143, 144]. Fig. 6 summarizes the observed X(gamma)-ray data. Most data sets are used to constrain the fermionic DM absorption operators for the first time with the only exception of HEAO-1 and INTEGRAL-08 [138]. The constraints on the DM decay width  $\Gamma_\chi$  are shown in Fig. 7 while the constraints on the interaction strength in terms of the direct detection cross section  $\sigma_{\chi e\nu_\chi}$  have already been included in Fig. 4 altogether.

To constrain the DM decay width  $\Gamma_\chi$ , we require the predicted photon events in each energy bin does not exceed the experimental counts at 95% C.L. In a single energy bin  $[E_i^-, E_i^+]$ , the constraint is obtained with

$$N_i^{\text{th}} \leq N_i^{\text{obs}} \equiv A_{\text{eff}} T_{\text{obs}} \Delta\Omega \left( \frac{d^2\Phi_\gamma}{dE_\gamma d\Omega} \right)_{\text{exp@95\%}}^i \Delta E_i. \quad (43)$$

In principle, one may directly compare the predicted flux  $d^2\Phi_\gamma/dE_\gamma d\Omega$  with the data in Fig. 6 without converting to event number in each bin. Nevertheless, the spectrum of the two-body channel  $\chi \rightarrow \nu\gamma$  for the tensor operator  $\mathcal{O}_{e\nu\chi}^T$  is a  $\delta$  function which is difficult to directly compare with Fig. 6. With multiple data points, we can obtain a corresponding limit for the decay width  $\Gamma_\chi^i$  from the  $i$ -th energy bin, and we take the strongest bound among all bins as the final limit for the corresponding mass point.

Some data releases, especially Insight-HXMT [139] and NuSTAR/M31 [141], even provide background models in addition to data points. This opens the possibility to use  $\chi^2$  fit to obtain enhanced sensitivity than simply comparing with the central value plus the 95% C.L. uncertainty for individual bins. Putting things together, the corresponding  $\chi^2$  function for fitting the NuSTAR/M31 data is,

$$\chi^2(x_i, \Lambda) \equiv \sum_i \left[ \frac{\Lambda_{\text{TeV}}^{-4} N_i^{\text{DM}}(\Lambda = 1 \text{ TeV}) + \sum_a c_a N_i^a - N_i^{\text{exp}}}{\delta N_i} \right]^2, \quad (44)$$

where  $\Lambda_{\text{TeV}} \equiv \Lambda/\text{TeV}$ . The observation data provides the central values  $N_i^{\text{exp}}$  and the corresponding uncertainty  $\delta N_i$  for the  $i$ -th bin. Each observation can have multiple backgrounds  $N_i^a$  with  $a$  denoting its type and  $c_a$  the corresponding normalization factor. The  $\chi^2$  fit with data takes  $c_a$  as fitting parameters while the one for the DM contribution is the cut-off scale  $\Lambda_{\text{TeV}}$  in unit of TeV. More details of the analytic  $\chi^2$  fit can be found in App. A.

Below is a detailed description of each data set and their constraints on the DM decay width and coupling strength.

- **Insight-HXMT/CXB:** We use the (1 ~ 12) keV cosmic X-ray background (CXB) data observed by the Low Energy X-ray Telescope on Insight-HXMT (Hard X-ray Modulation Telescope) [139]. The observation points to the sky in the direction  $(l, b) = (219.3^\circ, -50.0^\circ)$  with a small FOV ( $1.6^\circ \times 6^\circ$ ). The relevant effective detector area is taken from the Fig. 1 on the HXMT website [145]. For comparison, the background model for CXB is taken from the yellow line of the Fig. 11 therein. With both data points and background model provided, we use analytic  $\chi^2$  fit to obtain constraint. The result is shown in Fig. 7 with blue color. In the  $\mathcal{O}(1)$  keV range, Insight-HXMT/CXB gives a strong constraint.
- **NuSTAR/CXB:** The Fig. 10 of [140] gives the average CXB spectrum within the 3 ~ 20 keV energy range. This spectrum is obtained by stacking the focal plane module (FPM) A and B (FPMA and FPMB) observations with all six data sets (COSMOS EP1,2,3, EGS, ECDFS, UDS).

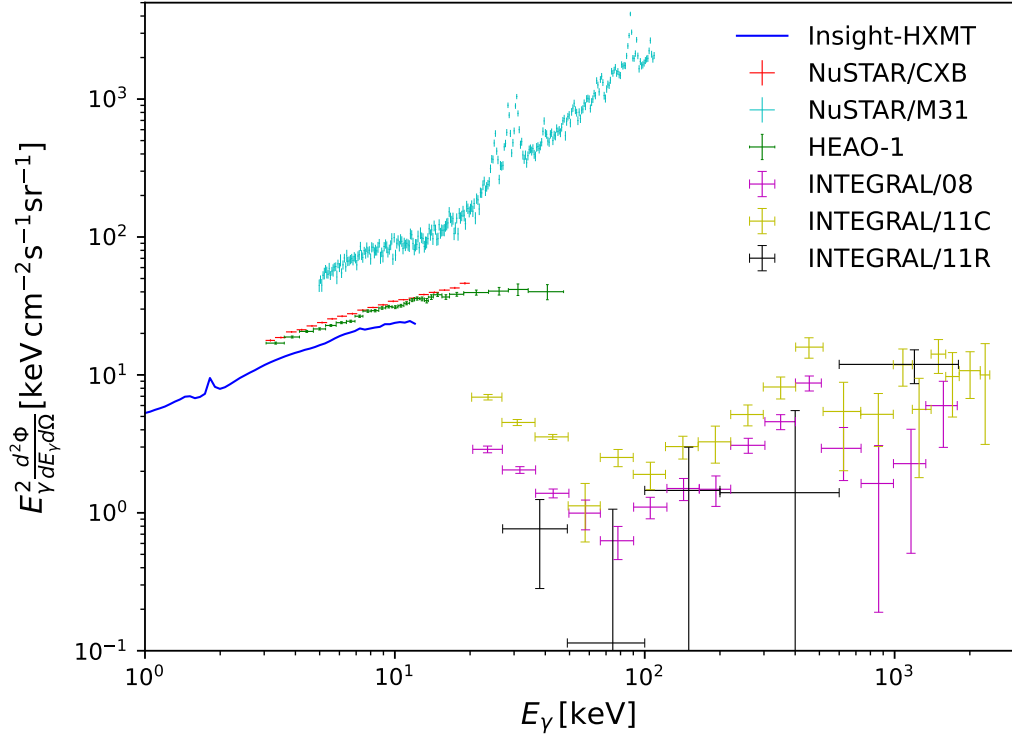


FIG. 6. The observed X(gamma)-ray fluxes by Insight-HXMT/CXB (blue) [139], NuSTAR/CMB (red) [140], NuSTAR/M31 (cyan) [141], HEAO-1 (green) [142], INTEGRAL (magenta, yellow, and black) [143, 144]. The three INTEGRAL data sets are released in 2008 (magenta) [143] and 2011 (yellow for 11C and black for 11R) [144] for different observational sky regions as described in the main text.

- **NuSTAR/M31:** In addition to the diffuse CXB, galaxy observation can also provide a strong constraint due to the concentrated DM density profile. A typical case is the NuSTAR observation of M31. We use the (5 ~ 100) keV data in the Fig. 2 of [141] from the observation ID 50026002003. The NuSTAR instrumental and solar contributions, the 0-bounce CXB component, and the 2-bounce component from the diffuse M31 emission are taken into consideration as backgrounds. The background models are taken from the fit curves in the Fig. 2 of [141]. Each component has its own normalization factor as fitting parameter. Since the 2-bounce CXB component is very small, we neglect it in our  $\chi^2$  fit to avoid numerical instability.

For the DM decay photons, the 0-bounce and 2-bounce DM decay photons have different effective areas. To properly take the 2-bounce contribution into account, we use the enhancement factor defined in [141],

$$\xi(E_\gamma) \equiv 1 + \frac{A_{2b}(E_\gamma)\Delta\Omega_{2b}\mathcal{J}_{2b}}{A_{0b}\Delta\Omega_{0b}\mathcal{J}_{0b}}. \quad (45)$$

Then the predicted DM decay photon events in each energy bin can be written as,

$$N_i^{\text{DM}} \equiv A_{0b}T_{\text{obs}}\Delta\Omega_{0b}\frac{\mathcal{J}_{0b}}{4\pi m_\chi} \int dE_\gamma \xi(E_\gamma) \frac{d\Gamma_\gamma}{dE_\gamma}, \quad (46)$$

where the observational effective area for the 0-bounce photons is  $A_{0b} = 11.85$  (11.80)  $\text{cm}^2$ , the exposure time is  $T_{\text{obs}} = 82.4$  (82.2) ks and the FOV  $\Delta\Omega_{0b} = 4.45$  (4.55)  $\text{deg}^2$  for the FPMA

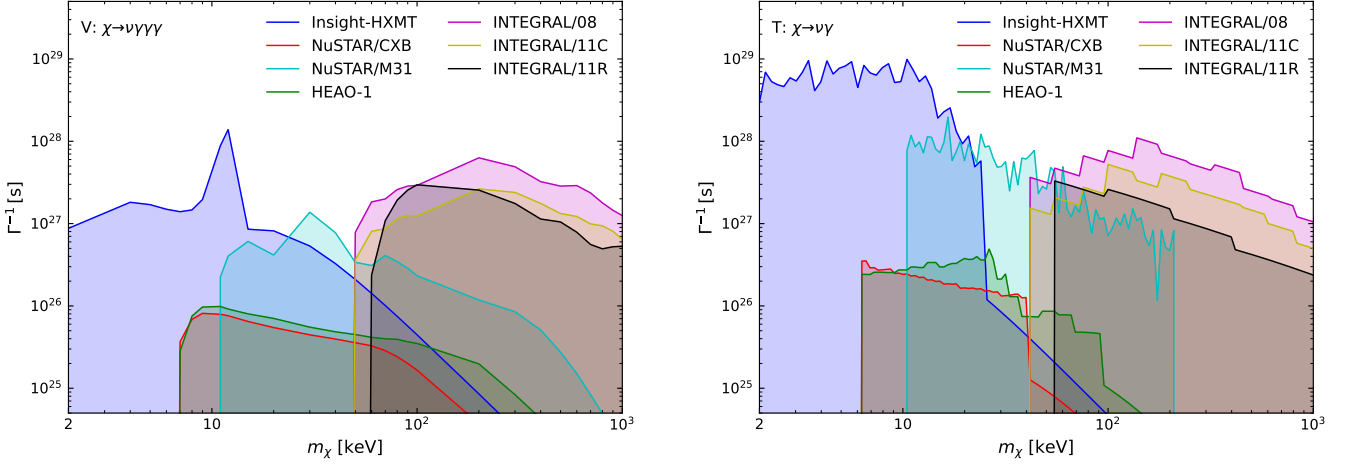


FIG. 7. The astrophysical X-ray and gamma-ray constraints on the visible decay width of  $\chi \rightarrow \nu + \gamma(s)$  as a function of the DM mass  $m_\chi$ . For illustration, the vector operator with continuum spectrum from  $\chi \rightarrow \nu\gamma\gamma$  and the tensor one with discrete  $\delta$ -function from  $\chi \rightarrow \nu\gamma$  are shown in the left and right panels, respectively.

(FPMB) observation, respectively. The DM decay factor  $\mathcal{J}_{0b} = 6.72 (7.13) \text{ GeV cm}^{-3} \text{ kpc sr}^{-1}$  for FPMA (FPMB) includes both the Milky Way and M31 contributions. One can neglect the extragalactic contribution which is much smaller.

- **HEAO-1:** The HEAO-1 extragalactic diffuse X-ray data in the Fig. 2 of [142] corresponds to the sky region  $l \in (58^\circ, 106^\circ) \cup (238^\circ, 289^\circ)$ ,  $|b| \in (20^\circ, 90^\circ)$ . Following [138], we only use the (3 ~ 50) keV data set observed by the A2 High-Energy Detector (HED).
- **INTEGRAL:** We use both the galactic center gamma-ray spectrum ( $|b| < 15^\circ$  and  $|l| < 30^\circ$ ) as well as the galactic ridge emission spectrum from the SPI measurements on board INTEGRAL. 1) There are two data sets for the galactic center gamma-ray spectrum with photon energy (20 ~ 2000) keV. One is from the Fig. 9 of [143] released in 2008 and shown as INTEGRAL/08 (magenta) in Fig. 6 while the other comes from the Fig. 6 of [144] released in 2011 and shown as INTEGRAL/11C (yellow). 2) For the galactic ridge emission spectrum, the Fig. 4 of [144] gives the diffuse emission as a function of galactic longitude with the latitude being integrated over and the Fig. 5 therein gives the one with the longitude being integrated over. The INTEGRAL measurements from this analysis are divided into five energy bins with divisions at  $E = (27, 49, 100, 200, 600, 1800) \text{ keV}$ , respectively. We select those bins that give the strongest limit and show their corresponding fluxes in Fig. 6 as INTEGRAL/11R (black).

Fig. 7 compiles all the astrophysical X-ray and gamma-ray constraints on the DM visible decay. While the photon energy is typically smaller than half of the DM mass,  $E_\gamma < m_\chi/2$ , the energy range (1 ~ 3000) keV in Fig. 6 covers the DM mass window (2 ~ 1000) keV in Fig. 7. Although there are three different decay channels,  $\chi \rightarrow (\nu\gamma, \nu\gamma\gamma, \nu\gamma\gamma\gamma)$ , the last two share similar features of continuum spectrum while the first has a discrete  $\delta$  function. For illustration purpose, we only show the vector and tensor cases in the left and right panels of Fig. 7, respectively. Due to this difference, the curves for the vector case are quite smooth while the tensor ones have many breaks and spikes. In addition, the tensor case typically has much clearer boundaries such as the NuSTAR/M31 curve. The results for  $\chi \rightarrow \nu\gamma\gamma$  are quite similar to those of  $\chi \rightarrow \nu\gamma\gamma\gamma$ .

It is interesting to observe that, although the NuSTAR/M31 flux in Fig. 6 is not as small as other observations, its constraint on the DM visible decay width is not bad and even better than some

others such as INTEGRAL. This is because the INTEGRAL constraints comes from comparing the theoretical prediction with all observed event counts plus errors at 95% C.L. while the NuSTAR/M31 constraint is comes from a more realistic  $\chi^2$  fit. If possible,  $\chi^2$  fit is more desirable although doing this for all astrophysical data is beyond the scope of the current paper.

Another important feature is that, the constraining power can go beyond the  $E_\gamma < m_\chi/2$  correspondence. Taking the Insight-HXMT curve for demonstration, the adopted spectrum spans the energy range (1 ~ 12) keV while the constrained mass range can extend up to  $\mathcal{O}(100)$  keV. This is because the extragalactic contributions from the vast Universe receive redshift to different extent. Although the emitted photon spectrum is fixed by the DM mass  $m_\chi$  and the decay vertex, the observed photon energy could be much lower. A heavier  $m_\chi$  above the energy window can also receive constraint from low energy X-ray observation.

The constraints in terms of the direct detection cross section  $\sigma_{\chi e \nu_\chi}$  have already been shown in Fig. 4 for comparison. Comparing with the overproduction constraints, the decay constraints are typically more stringent for heavier DM for both the invisible and visible channels. This is because the decay width typically grows with the DM mass. The constraint for the tensor operator is particularly strong since it comes from the single photon channel  $\chi \rightarrow \nu\gamma$  with much larger phase space. The next highly constrained operator is the pseudo-scalar type. Neither the freeze-in production nor decay process of the pseudo-scalar operator is suppressed for the others. So the constraints on its cut-off scale should be roughly the same as others. However, the direct detection cross section is highly suppressed for the pseudo-scalar case. Both pseudo-scalar and tensor operators are difficult to be directly probed. The constraints on the other operators are not that severe. Of them, the vector case is of particular interest for tonne-scale direct detection experiments (such as PandaX-4T [146, 147], XENONnT [148], and LZ [149, 150]) which will soon be able to probe small DM mass  $m_\chi$  of  $\mathcal{O}(10 \sim 100)$  keV that has not been excluded by cosmological or astrophysical constraints.

## VI. CONCLUSIONS

We systematically investigated the fermionic DM absorption on the electron target that allow unique probe of sub-MeV DM. Using the effective fermionic absorption operators, we found that the electron recoil spectrum in direct detection has roughly the same shape that is mainly determined by the atomic  $K$ -factor for different operators. This allows a model-independent, or at least operator-independent, measurement to some extent. It even allows in-situ measurement of the atomic  $K$ -factor if the fermionic DM absorption is confirmed. The only complication is that the pseudo-scalar case has quite different signal size. The comparison with the Xenon1T and PandaX-II electron recoil spectrum prefers a vector-type DM absorption with  $m_\chi = 59$  keV and 105 keV respectively. With the corresponding best-fit value  $\Lambda \approx 1$  TeV, the Xenon1T and PandaX-II can probe the new physics cut-off scale up to TeV scale. We also systematically update the overproduction, cosmological, and astrophysical constraints. Especially, the X(gamma)-ray constraints from the Insight-HXMT, NuSTAR, and INTEGRAL 2011 data sets are newly used to constrain the sub-MeV fermionic absorption DM. Even though the tensor and pseudo-scalar operators are strongly constrained, the fermionic DM absorption with other operator types is still testable at tonne-scale experiments.

## ACKNOWLEDGEMENTS

The authors would like to thank Roman Krivonos, Lei Lei, Jin-Yuan Liao, Jiang-Lai Liu, Dan Zhang, and Shuang-Nan Zhang for useful discussions. The authors thank Kenny C. Y. Ng for providing us the NuSTAR/M31 data, the  $\mathcal{J}$  factor and the enhancement factor of the 2 bounce

FOV in their paper [141]. The authors also thank Jeff A. Dror for double-checking the results in [105]. This work is supported in part by the Double First Class start-up fund (WF220442604), the Shanghai Pujiang Program (20PJ1407800), National Natural Science Foundation of China (Nos. 12090064, 11975149, 11735010), Chinese Academy of Sciences Center for Excellence in Particle Physics (CCEPP), and Key Laboratory for Particle Physics, Astrophysics and Cosmology, Ministry of Education, and Shanghai Key Laboratory for Particle Physics and Cosmology (Grant No. 15DZ2272100). XGH was also supported in part by the MOST (Grant No. MOST 106- 2112-M-002-003-MY3 ).

### Appendix A: Analytic $\chi^2$ Fit with Collective Marginalization

The fitting with experimental data points in this paper is achieved with analytical  $\chi^2$  fit [113, 114]. With Gaussian distribution, the  $\chi^2$  minimization is equivalent to matrix manipulation. Most importantly, the marginalization for a single parameter can also be done as matrix element manipulation to reduce a  $\chi^2$  function with  $n$  parameters to the one with  $n - 1$  parameters. This single-parameter marginalization needs to be done recursively in order to marginalize over multiple parameters. Here we provide a more elegant formalism to marginalize over multiple parameters collectively.

Given a set of observables  $\mathcal{O}_j$ , the  $\chi^2$  function can be generally parametrized as,

$$\chi^2 = \sum_j \left( \frac{\mathcal{O}_j^{\text{th}} - \mathcal{O}_j^{\text{exp}}}{\Delta \mathcal{O}_j} \right)^2, \quad (\text{A1})$$

where  $\mathcal{O}_j^{\text{th}}$  and  $\mathcal{O}_j^{\text{exp}}$  are the theoretical prediction and experimental observation for the  $j$ -th bin, respectively. A Gaussian  $\chi^2$  function is equivalent to linear dependence of  $\mathcal{O}_j^{\text{th}}$  on the model parameters  $x_i$ , ( $i = 1, 2, \dots, n$ ) as  $\mathcal{O}_j^{\text{th}} \approx \mathcal{O}_j^{\text{th},0} + \sum_i A_{ji} x_i$ . In matrix form, the  $\chi^2$  function can be written as

$$\chi^2(x_i) = (\mathcal{O}^{\text{th},0} + Ax - \mathcal{O}^{\text{exp}})^T \bar{\Sigma}^{-1} (\mathcal{O}^{\text{th},0} + Ax - \mathcal{O}^{\text{exp}}), \quad \bar{\Sigma}^{-1} \equiv \text{diag}(\Delta \mathcal{O}_j^{-2}). \quad (\text{A2})$$

For  $m$  observables and  $n$  fitting parameters,  $A$  is a  $m \times n$  constant coefficient matrix and  $x \equiv (x_1, \dots, x_n)^T$  is a  $n \times 1$  column vector. Then  $A$  converts the  $n \times 1$  parameter vector  $x$  to a  $m \times 1$  observable vector  $Ax$  that can match with  $\mathcal{O}^{\text{th},0}$  and  $\mathcal{O}^{\text{exp}}$ . Finally, the  $m \times m$  error matrix  $\bar{\Sigma}^{-1}$  in the observable space contracts with two observable vectors, one column and one row vectors, to produce a scalar  $\chi^2$  function. By definition, error matrix is symmetric.

The  $\chi^2$  minimization condition  $\partial \chi^2 / \partial x_i \equiv 0$  gives a unique solution for the best fit value of the fitting parameters,

$$x_{\text{best}} \equiv (A^T \bar{\Sigma}^{-1} A)^{-1} A^T \bar{\Sigma}^{-1} (\mathcal{O}^{\text{th},0} - \mathcal{O}^{\text{exp}}). \quad (\text{A3})$$

With larger deviation between the experimentally observed  $\mathcal{O}^{\text{exp}}$  and the zeroth-order prediction  $\mathcal{O}^{\text{th},0}$ , the fitting parameter should also deviate more from the one used to predict  $\mathcal{O}^{\text{th},0}$ . Correspondingly, the  $\chi^2$  function splits into two parts

$$\chi^2(x_i) = \chi_{\text{min}}^2 + (x - x_{\text{best}})^T \Sigma^{-1} (x - x_{\text{best}}), \quad (\text{A4})$$

Now  $\chi^2$  becomes a function of fitting parameters  $x_i$ , instead of observables, with the corresponding  $n \times n$  error matrix  $\Sigma^{-1} \equiv A^T \bar{\Sigma}^{-1} A$  in the parameter space. The first term of (A4) is the minimum value of the  $\chi^2$ ,

$$\chi_{\text{min}}^2 \equiv (\mathcal{O}^{\text{th},0} - \mathcal{O}^{\text{exp}})^T B^T \bar{\Sigma}^{-1} B (\mathcal{O}^{\text{th},0} - \mathcal{O}^{\text{exp}})^T, \quad B \equiv \mathbb{I} - A(A^T \bar{\Sigma}^{-1} A)^{-1} A^T \bar{\Sigma}^{-1}, \quad (\text{A5})$$

while the second is actually  $\delta\chi^2(x_i)$  as deviation from  $\chi_{\min}^2$ .

With multiple fitting parameters in (A4), it is difficult to see the probability distribution of any specific one. It is desirable to obtain the  $\chi^2$  of a single parameter by marginalizing over the others. This can be achieved by integrating out the unnecessary ones from the distribution function  $\mathbb{P}(x_1, \dots, x_n)$ . Taking one-parameter reduction for illustration,

$$\mathbb{P}(x_1, \dots, \hat{x}_k, \dots, x_n) = \int \mathbb{P}(x_1, \dots, x_n) dx_k, \quad (\text{A6})$$

where the  $k$ -th element is marginalized. For a Gaussian distribution, this is equivalent to matrix element manipulation of the error matrix  $\Sigma^{-1}$  in the parameter space,

$$\tilde{\Sigma}_{ij}^{-1} = \Sigma_{ij}^{-1} - \frac{\Sigma_{ik}^{-1} \Sigma_{jk}^{-1}}{\Sigma_{kk}^{-1}}. \quad (\text{A7})$$

While  $\Sigma^{-1}$  being a  $n \times n$  matrix,  $\tilde{\Sigma}^{-1}$  is  $(n-1) \times (n-1)$  after marginalizing one single parameter  $x_k$ . Keeping doing this repeatedly, one can finally arrive at a  $\chi^2$  function with only one parameter.

Nevertheless, this procedure is a little bit troublesome with  $n-1$  repetition when  $n$  becomes large. Below we provide a more convenient algorithm of collective marginalization which can reduce a  $n$ -parameter  $\chi^2$  function directly to a single-parameter one without repetition. Suppose one needs to marginalize over  $k$  parameters out of the original  $n$  ones. Instead of using a single  $n \times 1$  vector  $x$ , the fitting parameters can be separated into one  $(n-k) \times 1$  vector  $X$  that shall remain and one  $k \times 1$  vector  $Y$  that needs to be marginalized away. Correspondingly, the experimental observables is predicted as

$$\mathcal{O}^{\text{th},0} + A_X X + A_Y Y, \quad (\text{A8})$$

instead of the original  $\mathcal{O}^{\text{th},0} + Ax$ . The  $\chi^2$  function (A2) then becomes

$$\chi^2(X, Y) = (\mathcal{O}^{\text{th},0} + A_X X + A_Y Y - \mathcal{O}^{\text{exp}})^T \bar{\Sigma}^{-1} (\mathcal{O}^{\text{th},0} + A_X X + A_Y Y - \mathcal{O}^{\text{exp}}). \quad (\text{A9})$$

For convenience, one may define  $\delta\mathcal{O}_X \equiv \mathcal{O}^{\text{th},0} + A_X X - \mathcal{O}^{\text{exp}}$  and the  $\chi^2(X, Y)$  function becomes,

$$\chi^2(X, Y) = Y^T \Sigma_Y^{-1} Y + 2Y^T A_Y^T \bar{\Sigma}^{-1} \delta\mathcal{O}_X + \delta\mathcal{O}_X^T \bar{\Sigma}^{-1} \delta\mathcal{O}_X, \quad (\text{A10})$$

with  $\Sigma_Y^{-1} \equiv A_Y^T \bar{\Sigma}^{-1} A_Y$ . Only the first two terms are relevant in the Gaussian integration of the marginalization of  $Y$ ,

$$\mathbb{P}(X) = \int \mathbb{P}(X, Y) dY = N \int e^{-\frac{1}{2} \chi^2(X, Y)} dY, \quad (\text{A11})$$

with a normalization factor  $N$  that would not affect the probability distribution. The result would be more transparent by reforming (A10) as,

$$\begin{aligned} \chi^2(X, Y) &= (Y + \Sigma_Y A_Y^T \bar{\Sigma}^{-1} \delta\mathcal{O}_X)^T \Sigma_Y^{-1} (Y + \Sigma_Y A_Y^T \bar{\Sigma}^{-1} \delta\mathcal{O}_X) \\ &\quad + \delta\mathcal{O}_X^T \left[ \bar{\Sigma}^{-1} - \bar{\Sigma}^{-1} A_Y \Sigma_Y A_Y^T \bar{\Sigma}^{-1} \right] \delta\mathcal{O}_X. \end{aligned} \quad (\text{A12})$$

The first line is a Gaussian form of  $Y$  while the second line is independent of  $Y$ . Then the Gaussian integration (A11) gives,

$$\mathbb{P}(X) \propto \exp \left[ -\frac{1}{2} (\mathcal{O}^{\text{th},0} + A_X X - \mathcal{O}^{\text{exp}})^T \bar{\Sigma}_X^{-1} (\mathcal{O}^{\text{th},0} + A_X X - \mathcal{O}^{\text{exp}}) \right], \quad (\text{A13})$$



up to a normalization factor. Since a Gaussian probability distribution is defined as  $\mathbb{P}(X) \propto e^{-\chi^2(X)/2}$ , one can read off the reduced  $\chi^2(X)$  directly from the above equation. The reduced experimental error matrix,

$$\overline{\Sigma}_X^{-1} \equiv \overline{\Sigma}^{-1} - \overline{\Sigma}^{-1} A_Y \Sigma_Y A_Y^T \overline{\Sigma}^{-1}, \quad (\text{A14})$$

with only parameters  $X$  replaces the original  $\overline{\Sigma}^{-1}$ . It is interesting to observe that the reduced  $\chi^2(X)$  in (A13) resembles the original form (A2). The effect of  $Y$  parameters is wholly encoded in  $\overline{\Sigma}_X^{-1}$ . It not only affects the  $X$  error matrix,  $\Sigma_X^{-1} \equiv A_X^T \overline{\Sigma}_X^{-1} A_X$ , but also its best fit values. The marginalization down to a single parameter corresponds to  $k = n - 1$ .

- 
- [1] B. L. Young, “A survey of dark matter and related topics in cosmology,” *Front. Phys. (Beijing)* **12**, no.2, 121201 (2017) [erratum: *Front. Phys. (Beijing)* **12**, no.2, 121202 (2017)]
- [2] A. Arbey and F. Mahmoudi, “Dark matter and the early Universe: a review,” *Prog. Part. Nucl. Phys.* **119**, 103865 (2021) [arXiv:2104.11488 [hep-ph]].
- [3] J. Liu, X. Chen and X. Ji, “Current status of direct dark matter detection experiments,” *Nature Phys.* **13**, no.3, 212-216 (2017) [arXiv:1709.00688 [astro-ph.CO]].
- [4] J. Billard, M. Boulay, S. Cebrián, L. Covi, G. Fiorillo, A. Green, J. Kopp, B. Majorovits, K. Palladino and F. Petricca, *et al.* “Direct Detection of Dark Matter – APPEC Committee Report,” [arXiv:2104.07634 [hep-ex]].
- [5] R. K. Leane, “Indirect Detection of Dark Matter in the Galaxy,” [arXiv:2006.00513 [hep-ph]].
- [6] T. R. Slatyer, “Les Houches Lectures on Indirect Detection of Dark Matter,” [arXiv:2109.02696 [hep-ph]].
- [7] A. Albert, M. Bauer, J. Brooke, O. Buchmueller, D. G. Cerdeño, M. Citron, G. Davies, A. De Cosa, A. De Roeck and A. De Simone, *et al.* “Towards the next generation of simplified Dark Matter models,” *Phys. Dark Univ.* **16**, 49-70 (2017) [arXiv:1607.06680 [hep-ex]].
- [8] K. Arun, S. B. Gudennavar and C. Sivaram, “Dark matter, dark energy, and alternate models: A review,” *Adv. Space Res.* **60**, 166-186 (2017) [arXiv:1704.06155 [physics.gen-ph]].
- [9] T. Lin, “Dark matter models and direct detection,” *PoS* **333**, 009 (2019) [arXiv:1904.07915 [hep-ph]].
- [10] L. Roszkowski, E. M. Sessolo and S. Trojanowski, “WIMP dark matter candidates and searches—current status and future prospects,” *Rept. Prog. Phys.* **81**, no.6, 066201 (2018) [arXiv:1707.06277 [hep-ph]].
- [11] S. Bottaro, D. Buttazzo, M. Costa, R. Franceschini, P. Panci, D. Redigolo and L. Vittorio, “Closing the window on WIMP Dark Matter,” *Eur. Phys. J. C* **82**, no.1, 31 (2022) [arXiv:2107.09688 [hep-ph]].
- [12] J. H. Davis, “The Past and Future of Light Dark Matter Direct Detection,” *Int. J. Mod. Phys. A* **30**, no.15, 1530038 (2015) [arXiv:1506.03924 [hep-ph]].
- [13] M. Drewes, T. Lasserre, A. Merle, S. Mertens, R. Adhikari, M. Agostini, N. A. Ky, T. Araki, M. Archidiacono and M. Bahr, *et al.* “A White Paper on keV Sterile Neutrino Dark Matter,” *JCAP* **01**, 025 (2017) [arXiv:1602.04816 [hep-ph]].
- [14] K. N. Abazajian, “Sterile neutrinos in cosmology,” *Phys. Rept.* **711-712**, 1-28 (2017) [arXiv:1705.01837 [hep-ph]].
- [15] A. Boyarsky, M. Drewes, T. Lasserre, S. Mertens and O. Ruchayskiy, “Sterile neutrino Dark Matter,” *Prog. Part. Nucl. Phys.* **104**, 1-45 (2019) [arXiv:1807.07938 [hep-ph]].
- [16] J. Kopp, “Sterile Neutrinos as Dark Matter Candidates,” *Les Houches summer school on Dark Matter* [arXiv:2109.00767 [hep-ph]].
- [17] N. Bozorgnia, F. Calore, M. Schaller, M. Lovell, G. Bertone, C. S. Frenk, R. A. Crain, J. F. Navarro, J. Schaye and T. Theuns, “Simulated Milky Way analogues: implications for dark matter direct searches,” *JCAP* **05**, 024 (2016) [arXiv:1601.04707 [astro-ph.CO]].
- [18] J. I. Collar, A. R. L. Kavner and C. M. Lewis, “Germanium response to sub-keV nuclear recoils: a multipronged experimental characterization,” *Phys. Rev. D* **103**, no.12, 122003 (2021) [arXiv:2102.10089 [nucl-ex]].
- [19] S. Pirro and P. Mauskopf, “Advances in Bolometer Technology for Fundamental Physics,” *Ann. Rev. Nucl. Part. Sci.* **67**, 161-181 (2017);
- [20] A. H. Abdelhameed *et al.* [CRESST], “First results from the CRESST-III low-mass dark matter program,” *Phys. Rev. D* **100**, no.10, 102002 (2019) [arXiv:1904.00498 [astro-ph.CO]].
- [21] C. Kouvaris and J. Pradler, “Probing sub-GeV Dark Matter with conventional detectors,” *Phys. Rev. Lett.* **118**, no.3, 031803 (2017) [arXiv:1607.01789 [hep-ph]].
- [22] G. Grilli di Cortona, A. Messina and S. Piacentini, “Migdal effect and photon Bremsstrahlung: improving the sensitivity to light dark matter of liquid argon experiments,” *JHEP* **11**, 034 (2020) [arXiv:2006.02453 [hep-ph]].
- [23] M. Ibe, W. Nakano, Y. Shoji and K. Suzuki, “Migdal Effect in Dark Matter Direct Detection Experiments,” *JHEP* **03**, 194 (2018) [arXiv:1707.07258 [hep-ph]].
- [24] D. Baxter, Y. Kahn and G. Krnjaic, “Electron Ionization via Dark Matter-Electron Scattering and the Migdal Effect,” *Phys. Rev. D* **101**, no.7, 076014 (2020) [arXiv:1908.00012 [hep-ph]].
- [25] R. Essig, J. Pradler, M. Sholapurkar and T. T. Yu, “Relation between the Migdal Effect and Dark Matter-Electron

- Scattering in Isolated Atoms and Semiconductors*,” *Phys. Rev. Lett.* **124**, no.2, 021801 (2020) [arXiv:1908.10881 [hep-ph]].
- [26] U. K. Dey, T. N. Maity and T. S. Ray, “*Prospects of Migdal Effect in the Explanation of XENON1T Electron Recoil Excess*,” *Phys. Lett. B* **811**, 135900 (2020) [arXiv:2006.12529 [hep-ph]].
- [27] C. P. Liu, C. P. Wu, H. C. Chi and J. W. Chen, “*Model-independent determination of the Migdal effect via photoabsorption*,” *Phys. Rev. D* **102**, no.12, 121303 (2020) [arXiv:2007.10965 [hep-ph]].
- [28] K. D. Nakamura, K. Miuchi, S. Kazama, Y. Shoji, M. Ibe and W. Nakano, “*Detection capability of the Migdal effect for argon and xenon nuclei with position-sensitive gaseous detectors*,” *PTEP* **2021**, no.1, 013C01 (2021) [arXiv:2009.05939 [physics.ins-det]].
- [29] S. Knapen, J. Kozacuk and T. Lin, “*Migdal Effect in Semiconductors*,” *Phys. Rev. Lett.* **127**, no.8, 081805 (2021) [arXiv:2011.09496 [hep-ph]].
- [30] V. V. Flambaum, L. Su, L. Wu and B. Zhu, “*Constraining sub-GeV dark matter from Migdal and Boosted effects*,” [arXiv:2012.09751 [hep-ph]].
- [31] N. F. Bell, J. B. Dent, B. Dutta, S. Ghosh, J. Kumar and J. L. Newstead, “*Low-mass inelastic dark matter direct detection via the Migdal effect*,” *Phys. Rev. D* **104**, no.7, 7 (2021) [arXiv:2103.05890 [hep-ph]].
- [32] J. F. Acevedo, J. Bramante and A. Goodman, “*Accelerating composite dark matter discovery with nuclear recoils and the Migdal effect*,” *Phys. Rev. D* **105**, no.2, 023012 (2022) [arXiv:2108.10889 [hep-ph]].
- [33] W. Wang, K. Y. Wu, L. Wu and B. Zhu, “*Direct Detection of Spin-Dependent Sub-GeV Dark Matter via Migdal Effect*,” [arXiv:2112.06492 [hep-ph]].
- [34] **[Superheated Liquid]** V. Zacek, “*Search for dark matter with moderately superheated liquids*,” *Nuovo Cim. A* **107**, 291-298 (1994).
- [35] **[Superconductor]** Y. Hochberg, Y. Zhao and K. M. Zurek, “*Superconducting Detectors for Superlight Dark Matter*,” *Phys. Rev. Lett.* **116**, no.1, 011301 (2016) [arXiv:1504.07237 [hep-ph]].
- [36] **[Fermi-degenerate Material]** Y. Hochberg, M. Pyle, Y. Zhao and K. M. Zurek, “*Detecting Superlight Dark Matter with Fermi-Degenerate Materials*,” *JHEP* **08**, 057 (2016) [arXiv:1512.04533 [hep-ph]].
- [37] **[Superfluid]** K. Schutz and K. M. Zurek, “*Detectability of Light Dark Matter with Superfluid Helium*,” *Phys. Rev. Lett.* **117**, no.12, 121302 (2016) [arXiv:1604.08206 [hep-ph]]; S. Knapen, T. Lin and K. M. Zurek, “*Light Dark Matter in Superfluid Helium: Detection with Multi-excitation Production*,” *Phys. Rev. D* **95**, no.5, 056019 (2017) [arXiv:1611.06228 [hep-ph]].
- [38] **[Scintillator]** S. Derenzo, R. Essig, A. Massari, A. Soto and T. T. Yu, “*Direct Detection of sub-GeV Dark Matter with Scintillating Targets*,” *Phys. Rev. D* **96**, no.1, 016026 (2017) [arXiv:1607.01009 [hep-ph]].
- [39] **[Magnetic Molecular]** P. C. Bunting, G. Gratta, T. Melia and S. Rajendran, “*Magnetic Bubble Chambers and Sub-GeV Dark Matter Direct Detection*,” *Phys. Rev. D* **95**, no.9, 095001 (2017) [arXiv:1701.06566 [hep-ph]].
- [40] **[Dirac Material]** Y. Hochberg, Y. Kahn, M. Lisanti, K. M. Zurek, A. G. Grushin, R. Ilan, S. M. Griffin, Z. F. Liu, S. F. Weber and J. B. Neaton, “*Detection of sub-MeV Dark Matter with Three-Dimensional Dirac Materials*,” *Phys. Rev. D* **97**, no.1, 015004 (2018) [arXiv:1708.08929 [hep-ph]].
- [41] **[Diamond]** N. A. Kurinsky, T. C. Yu, Y. Hochberg and B. Cabrera, “*Diamond Detectors for Direct Detection of Sub-GeV Dark Matter*,” *Phys. Rev. D* **99**, no.12, 123005 (2019) [arXiv:1901.07569 [hep-ex]].
- [42] **[Nanowire]** Y. Hochberg, I. Charaev, S. W. Nam, V. Verma, M. Colangelo and K. K. Berggren, “*Detecting Sub-GeV Dark Matter with Superconducting Nanowires*,” *Phys. Rev. Lett.* **123**, no.15, 151802 (2019) [arXiv:1903.05101 [hep-ph]].
- [43] **[Nanotube]** G. Cavoto, E. N. M. Cirillo, F. Cocina, J. Ferretti and A. D. Polosa, “*WIMP detection and slow ion dynamics in carbon nanotube arrays*,” *Eur. Phys. J. C* **76**, no.6, 349 (2016) [arXiv:1602.03216 [physics.ins-det]]; G. Cavoto, F. Luchetta and A. D. Polosa, “*Sub-GeV Dark Matter Detection with Electron Recoils in Carbon Nanotubes*,” *Phys. Lett. B* **776**, 338-344 (2018) [arXiv:1706.02487 [hep-ph]].
- [44] **[Magnon]** T. Trickle, Z. Zhang and K. M. Zurek, “*Direct Detection of Light Dark Matter with Magnons*,” [arXiv:1905.13744 [hep-ph]]; S. Chigusa, T. Moroi and K. Nakayama, “*Detecting Light Boson Dark Matter through Conversion into Magnon*,” [arXiv:2001.10666 [hep-ph]].
- [45] **[Graphene]** S. Y. Wang, “*Graphene-based detectors for directional dark matter detection*,” *Eur. Phys. J. C* **79**, no.7, 561 (2019) [arXiv:1509.08801 [physics.ins-det]]; D. Kim, J. C. Park, K. C. Fong and G. H. Lee, “*Detecting keV-Range Super-Light Dark Matter Using Graphene Josephson Junction*,” [arXiv:2002.07821 [hep-ph]].
- [46] **[Plasmon]** N. Kurinsky, D. Baxter, Y. Kahn and G. Krnjaic, “*A Dark Matter Interpretation of Excesses in Multiple Direct Detection Experiments*,” [arXiv:2002.06937 [hep-ph]].
- [47] **[Skipper CCD]** R. Essig, M. Fernandez-Serra, J. Mardon, A. Soto, T. Volansky and T. T. Yu, “*Direct Detection of sub-GeV Dark Matter with Semiconductor Targets*,” *JHEP* **05**, 046 (2016) [arXiv:1509.01598 [hep-ph]]; E. Andersson, A. Böckmark, R. Catena, T. Emken, H. K. Moberg and E. Åstrand, “*Projected sensitivity to sub-GeV dark matter of next-generation semiconductor detectors*,” *JCAP* **05**, 036 (2020) [arXiv:2001.08910 [hep-ph]]; P. Du, D. Egana-Ugrinovic, R. Essig and M. Sholapurkar, “*Sources of Low-Energy Events in Low-Threshold Dark-Matter and Neutrino Detectors*,” *Phys. Rev. X* **12**, no.1, 011009 (2022) [arXiv:2011.13939 [hep-ph]].
- [48] **[DNA]** C. A. J. O’Hare, V. G. Matsos, J. Newton, K. Smith, J. Hochstetter, R. Jaiswar, W. Kyaw, A. McNamara, Z. Kuncic and S. N. Grellscheid, *et al.* “*Particle detection and tracking with DNA*,” [arXiv:2105.11949 [physics.ins-det]].
- [49] C. V. Cappiello, K. C. Ng and J. F. Beacom, “*Reverse Direct Detection: Cosmic Ray Scattering With Light Dark Matter*,” *Phys. Rev. D* **99**, no.6, 063004 (2019) [arXiv:1810.07705 [hep-ph]].
- [50] T. Bringmann and M. Pospelov, “*Novel direct detection constraints on light dark matter*,” *Phys. Rev. Lett.* **122**, no. 17, 171801 (2019) [arXiv:1810.10543 [hep-ph]].

- [51] Y. Ema, F. Sala and R. Sato, “*Light Dark Matter at Neutrino Experiments*,” *Phys. Rev. Lett.* **122**, no.18, 181802 (2019) [[arXiv:1811.00520](#) [hep-ph]].
- [52] J. B. Dent, B. Dutta, J. L. Newstead and I. M. Shoemaker, “*Bounds on Cosmic Ray-Boosted Dark Matter in Simplified Models and its Corresponding Neutrino-Floor*,” *Phys. Rev. D* **101**, no.11, 116007 (2020) [[arXiv:1907.03782](#) [hep-ph]].
- [53] W. Wang, L. Wu, J. M. Yang, H. Zhou and B. Zhu, “*Cosmic ray boosted sub-GeV gravitationally interacting dark matter in direct detection*,” *JHEP* **12**, 072 (2020) [erratum: *JHEP* **02**, 052 (2021)] [[arXiv:1912.09904](#) [hep-ph]].
- [54] S. F. Ge, J. Liu, Q. Yuan and N. Zhou, “*Diurnal Effect of Sub-GeV Dark Matter Boosted by Cosmic Rays*,” *Phys. Rev. Lett.* **126**, no.9, 091804 (2021) [[arXiv:2005.09480](#) [hep-ph]].
- [55] Q. H. Cao, R. Ding and Q. F. Xiang, “*Searching for sub-MeV boosted dark matter from xenon electron direct detection*,” *Chin. Phys. C* **45**, no.4, 045002 (2021) [[arXiv:2006.12767](#) [hep-ph]].
- [56] W. Cho, K. Y. Choi and S. M. Yoo, “*Searching for boosted dark matter mediated by a new gauge boson*,” *Phys. Rev. D* **102**, no.9, 095010 (2020) [[arXiv:2007.04555](#) [hep-ph]].
- [57] Z. H. Lei, J. Tang and B. L. Zhang, “*Constraints on cosmic-ray boosted DM in CDEX-10*,” [[arXiv:2008.07116](#) [hep-ph]].
- [58] C. Xia, Y. H. Xu and Y. F. Zhou, “*Constraining light dark matter upscattered by ultrahigh-energy cosmic rays*,” *Nucl. Phys. B* **969**, 115470 (2021) [[arXiv:2009.00353](#) [hep-ph]].
- [59] J. B. Dent, B. Dutta, J. L. Newstead, I. M. Shoemaker and N. T. Arellano, “*Present and future status of light dark matter models from cosmic-ray electron upscattering*,” *Phys. Rev. D* **103**, 095015 (2021) [[arXiv:2010.09749](#) [hep-ph]].
- [60] N. F. Bell, J. B. Dent, B. Dutta, S. Ghosh, J. Kumar, J. L. Newstead and I. M. Shoemaker, “*Cosmic-ray upscattered inelastic dark matter*,” *Phys. Rev. D* **104**, 076020 (2021) [[arXiv:2108.00583](#) [hep-ph]].
- [61] J. C. Feng, X. W. Kang, C. T. Lu, Y. L. S. Tsai and F. S. Zhang, “*Revising inelastic dark matter direct detection by including the cosmic ray acceleration*,” [[arXiv:2110.08863](#) [hep-ph]].
- [62] Y. Chen, B. Fornal, P. Sandick, J. Shu, X. Xue, Y. Zhao and J. Zong, “*Earth Shielding and Daily Modulation from Electrophilic Boosted Dark Matter*,” [[arXiv:2110.09685](#) [hep-ph]].
- [63] W. Wang, W. N. Yang and B. Zhu, “*The Spin-dependent Scattering of Boosted Dark Matter*,” [[arXiv:2111.04000](#) [hep-ph]].
- [64] C. Xia, Y. H. Xu and Y. F. Zhou, “*Production and attenuation of cosmic-ray boosted dark matter*,” [[arXiv:2111.05559](#) [hep-ph]].
- [65] X. Cui *et al.* [PandaX-II], “*A Search for the Cosmic Ray Boosted Sub-GeV Dark Matter at the PandaX-II Experiment*,” [[arXiv:2112.08957](#) [hep-ex]].
- [66] R. Xu *et al.* [CDEX], “*Constraints on sub-GeV Dark Matter Boosted by Cosmic Rays from CDEX-10 Experiment at the China Jinping Underground Laboratory*,” [[arXiv:2201.01704](#) [hep-ex]].
- [67] C. V. Cappiello and J. F. Beacom, “*Strong New Limits on Light Dark Matter from Neutrino Experiments*,” *Phys. Rev. D* **100**, no.10, 103011 (2019) [erratum: *Phys. Rev. D* **104**, no.6, 069901 (2021)] [[arXiv:1906.11283](#) [hep-ph]].
- [68] G. Guo, Y. L. S. Tsai and M. R. Wu, “*Probing cosmic-ray accelerated light dark matter with IceCube*,” *JCAP* **10**, 049 (2020) [[arXiv:2004.03161](#) [astro-ph.HE]].
- [69] Y. Ema, F. Sala and R. Sato, “*Neutrino experiments probe hadrophilic light dark matter*,” *SciPost Phys.* **10**, no.3, 072 (2021) [[arXiv:2011.01939](#) [hep-ph]].
- [70] M. Andriamirado *et al.* [PROSPECT and (PROSPECT Collaboration)\*], “*Limits on sub-GeV dark matter from the PROSPECT reactor antineutrino experiment*,” *Phys. Rev. D* **104**, no.1, 012009 (2021) [[arXiv:2104.11219](#) [hep-ex]].
- [71] B. Chauhan, B. Dasgupta and A. Dighe, “*Large Energy Singles at JUNO from Atmospheric Neutrinos and Dark Matter*,” [[arXiv:2111.14586](#) [hep-ph]].
- [72] G. Guo, Y. L. S. Tsai, M. R. Wu and Q. Yuan, “*Elastic and Inelastic Scattering of Cosmic-Rays on Sub-GeV Dark Matter*,” *Phys. Rev. D* **102**, no.10, 103004 (2020) [[arXiv:2008.12137](#) [astro-ph.HE]].
- [73] S. Pandey, S. Karmakar and S. Rakshit, “*Interactions of astrophysical neutrinos with dark matter: a model building perspective*,” *JHEP* **01**, 095 (2019) [erratum: *JHEP* **11**, 215 (2021)] [[arXiv:1810.04203](#) [hep-ph]].
- [74] Y. Zhang, “*Speeding Up Dark Matter With Solar Neutrinos*,” *PTEP* **2022**, 013 [[arXiv:2001.00948](#) [hep-ph]].
- [75] Y. Jho, J. C. Park, S. C. Park and P. Y. Tseng, “*Cosmic-Neutrino-Boosted Dark Matter ( $\nu$ BDM)*,” [[arXiv:2101.11262](#) [hep-ph]].
- [76] A. Das and M. Sen, “*Boosted dark matter from diffuse supernova neutrinos*,” *Phys. Rev. D* **104**, no.7, 075029 (2021) [[arXiv:2104.00027](#) [hep-ph]].
- [77] W. Chao, T. Li and J. Liao, “*Connecting Primordial Black Hole to boosted sub-GeV Dark Matter through neutrino*,” [[arXiv:2108.05608](#) [hep-ph]].
- [78] D. Ghosh, A. Guha and D. Sachdeva, “*Exclusion limits on Dark Matter-Neutrino Scattering Cross-section*,” [[arXiv:2110.00025](#) [hep-ph]].
- [79] J. W. Wang, A. Granelli and P. Ullio, “*Direct Detection Constraints on Blazar-Boosted Dark Matter*,” [[arXiv:2111.13644](#) [astro-ph.HE]].
- [80] J. Alvey, M. Campos, M. Fairbairn and T. You, “*Detecting Light Dark Matter via Inelastic Cosmic Ray Collisions*,” *Phys. Rev. Lett.* **123**, 261802 (2019) [[arXiv:1905.05776](#) [hep-ph]].
- [81] R. Plestid, V. Takhistov, Y. D. Tsai, T. Bringmann, A. Kusenko and M. Pospelov, “*New Constraints on Millicharged Particles from Cosmic-ray Production*,” [[arXiv:2002.11732](#) [hep-ph]].
- [82] M. Kachelriess and J. Tjemsland, “*Meson production in air showers and the search for light exotic particles*,” *Astropart. Phys.* **132**, 102622 (2021) [[arXiv:2104.06811](#) [hep-ph]].
- [83] C. Kouvaris, “*Probing Light Dark Matter via Evaporation from the Sun*,” *Phys. Rev. D* **92**, no.7, 075001 (2015) [[arXiv:1506.04316](#) [hep-ph]].
- [84] H. An, M. Pospelov, J. Pradler and A. Ritz, “*Directly Detecting MeV-scale Dark Matter via Solar Reflection*,” *Phys. Rev.*

- Lett.* **120**, no.14, 141801 (2018) [erratum: *Phys. Rev. Lett.* **121**, no.25, 259903 (2018)] [arXiv:1708.03642 [hep-ph]].
- [85] T. Emken, C. Kouvaris and N. G. Nielsen, “*The Sun as a sub-GeV Dark Matter Accelerator*,” *Phys. Rev. D* **97**, no.6, 063007 (2018) [arXiv:1709.06573 [hep-ph]].
- [86] Y. Chen, M. Y. Cui, J. Shu, X. Xue, G. W. Yuan and Q. Yuan, “*Sun heated MeV-scale dark matter and the XENON1T electron recoil excess*,” *JHEP* **04**, 282 (2021) [arXiv:2006.12447 [hep-ph]].
- [87] T. Emken, “*Solar reflection of light dark matter with heavy mediators*,” [arXiv:2102.12483 [hep-ph]].
- [88] H. An, H. Nie, M. Pospelov, J. Pradler and A. Ritz, “*Solar reflection of dark matter*,” *Phys. Rev. D* **104**, no.10, 103026 (2021) [arXiv:2108.10332 [hep-ph]].
- [89] K. Agashe, Y. Cui, L. Necib and J. Thaler, “*(In)direct Detection of Boosted Dark Matter*,” *JCAP* **10**, 062 (2014) [arXiv:1405.7370 [hep-ph]].
- [90] J. Berger, Y. Cui and Y. Zhao, “*Detecting Boosted Dark Matter from the Sun with Large Volume Neutrino Detectors*,” *JCAP* **02**, 005 (2015) [arXiv:1410.2246 [hep-ph]].
- [91] J. F. Cherry, M. T. Frandsen and I. M. Shoemaker, “*Direct Detection Phenomenology in Models Where the Products of Dark Matter Annihilation Interact with Nuclei*,” *Phys. Rev. Lett.* **114**, 231303 (2015) [arXiv:1501.03166 [hep-ph]].
- [92] X. Chen and L. Yang, “*Search for boosted dark matter with high-Z material in underground experiments*,” [arXiv:2002.04995 [hep-ph]].
- [93] B. Fornal, P. Sandick, J. Shu, M. Su and Y. Zhao, “*Boosted Dark Matter Interpretation of the XENON1T Excess*,” *Phys. Rev. Lett.* **125**, no.16, 161804 (2020) [arXiv:2006.11264 [hep-ph]].
- [94] M. Pospelov, A. Ritz and M. B. Voloshin, “*Bosonic super-WIMPs as keV-scale dark matter*,” *Phys. Rev. D* **78**, 115012 (2008) [arXiv:0807.3279 [hep-ph]].
- [95] H. An, M. Pospelov, J. Pradler and A. Ritz, “*Direct Detection Constraints on Dark Photon Dark Matter*,” *Phys. Lett. B* **747**, 331-338 (2015) [arXiv:1412.8378 [hep-ph]].
- [96] Y. Hochberg, T. Lin and K. M. Zurek, “*Detecting Ultralight Bosonic Dark Matter via Absorption in Superconductors*,” *Phys. Rev. D* **94**, no.1, 015019 (2016) [arXiv:1604.06800 [hep-ph]].
- [97] Y. Hochberg, T. Lin and K. M. Zurek, “*Absorption of light dark matter in semiconductors*,” *Phys. Rev. D* **95**, no.2, 023013 (2017) [arXiv:1608.01994 [hep-ph]].
- [98] I. M. Bloch, R. Essig, K. Tobioka, T. Volansky and T. T. Yu, “*Searching for Dark Absorption with Direct Detection Experiments*,” *JHEP* **06**, 087 (2017) [arXiv:1608.02123 [hep-ph]].
- [99] D. Green and S. Rajendran, “*The Cosmology of Sub-MeV Dark Matter*,” *JHEP* **10**, 013 (2017) [arXiv:1701.08750 [hep-ph]].
- [100] A. Arvanitaki, S. Dimopoulos and K. Van Tilburg, “*Resonant absorption of bosonic dark matter in molecules*,” *Phys. Rev. X* **8**, no.4, 041001 (2018) [arXiv:1709.05354 [hep-ph]].
- [101] B. von Krosigk, M. J. Wilson, C. Stanford, B. Cabrera, R. Calkins, D. Jardin, N. A. Kurinsky, F. Ponce and C. P. Wu, “*Effect on dark matter exclusion limits from new silicon photoelectric absorption measurements*,” *Phys. Rev. D* **104**, no.6, 063002 (2021) [arXiv:2010.15874 [hep-ex]].
- [102] A. Mitridate, T. Trickle, Z. Zhang and K. M. Zurek, “*Dark matter absorption via electronic excitations*,” *JHEP* **09**, 123 (2021) [arXiv:2106.12586 [hep-ph]].
- [103] J. A. Dror, G. Elor and R. McGehee, “*Directly Detecting Signals from Absorption of Fermionic Dark Matter*,” *Phys. Rev. Lett.* **124**, no.18, 18 (2020) [arXiv:1905.12635 [hep-ph]].
- [104] J. A. Dror, G. Elor and R. McGehee, “*Absorption of Fermionic Dark Matter by Nuclear Targets*,” *JHEP* **02**, 134 (2020) [arXiv:1908.10861 [hep-ph]].
- [105] J. A. Dror, G. Elor, R. McGehee and T. T. Yu, “*Absorption of sub-MeV fermionic dark matter by electron targets*,” *Phys. Rev. D* **103**, no.3, 035001 (2021) [arXiv:2011.01940 [hep-ph]].
- [106] E. Aprile *et al.* [XENON], “*Excess electronic recoil events in XENON1T*,” *Phys. Rev. D* **102**, no.7, 072004 (2020) [arXiv:2006.09721 [hep-ex]].
- [107] C. Cheng *et al.* [PandaX-II], “*Search for Light Dark Matter-Electron Scatterings in the PandaX-II Experiment*,” *Phys. Rev. Lett.* **126**, no.21, 211803 (2021) [arXiv:2101.07479 [hep-ex]].
- [108] J. F. Nieves and P. B. Pal, “*Generalized Fierz identities*,” *Am. J. Phys.* **72**, 1100-1108 (2004) [arXiv:hep-ph/0306087 [hep-ph]].
- [109] C. C. Nishi, “*Simple derivation of general Fierz-type identities*,” *Am.J.Phys.* **73**, 1160-1163 (2005) [arXiv:hep-ph/0412245 [hep-ph]].
- [110] Y. Liao and J. Y. Liu, “*Generalized Fierz Identities and Applications to Spin-3/2 Particles*,” *Eur. Phys. J. Plus* **127**, 121 (2012) [arXiv:1206.5141 [hep-ph]].
- [111] S. F. Ge, P. Pasquini and J. Sheng, “*Solar Active-Sterile Neutrino Conversion with Atomic Effects at Dark Matter Direct Detection Experiments*,” [arXiv:2112.05560 [hep-ph]].
- [112] X. Zhou *et al.* [PandaX-II], “*A Search for Solar Axions and Anomalous Neutrino Magnetic Moment with the Complete PandaX-II Data*,” *Chin. Phys. Lett.* **38**, no.1, 011301 (2021) [arXiv:2008.06485 [hep-ex]].
- [113] S. F. Ge, K. Hagiwara, N. Okamura and Y. Takaesu, “*Determination of mass hierarchy with medium baseline reactor neutrino experiments*,” *JHEP* **05**, 131 (2013) [arXiv:1210.8141 [hep-ph]].
- [114] S. F. Ge, H. J. He and R. Q. Xiao, “*Probing new physics scales from Higgs and electroweak observables at  $e^+ e^-$  Higgs factory*,” *JHEP* **10**, 007 (2016) [arXiv:1603.03385 [hep-ph]].
- [115] E. W. Kolb and M. S. Turner, “*The Early Universe*,” *Front. Phys.* **69**, 1-547 (1990)
- [116] N. Bernal, M. Heikinheimo, T. Tenkanen, K. Tuominen and V. Vasconen, “*The Dawn of FIMP Dark Matter: A Review of Models and Constraints*,” *Int. J. Mod. Phys. A* **32**, no.27, 1730023 (2017) [arXiv:1706.07442 [hep-ph]].
- [117] T. Asaka, K. Ishiwata and T. Moroi, “*Right-handed sneutrino as cold dark matter*,” *Phys. Rev. D* **73**, 051301 (2006)

- [arXiv:hep-ph/0512118 [hep-ph]].
- [118] S. Gopalakrishna, A. de Gouvea and W. Porod, “*Right-handed sneutrinos as nonthermal dark matter*,” *JCAP* **05**, 005 (2006) [arXiv:hep-ph/0602027 [hep-ph]].
- [119] T. Asaka, K. Ishiwata and T. Moroi, “*Right-handed sneutrino as cold dark matter of the universe*,” *Phys. Rev. D* **75**, 065001 (2007) [arXiv:hep-ph/0612211 [hep-ph]].
- [120] V. Page, “*Non-thermal right-handed sneutrino dark matter and the  $\Omega_{DM}/\Omega_b$  problem*,” *JHEP* **04**, 021 (2007) [arXiv:hep-ph/0701266 [hep-ph]].
- [121] L. J. Hall, K. Jedamzik, J. March-Russell and S. M. West, “*Freeze-In Production of FIMP Dark Matter*,” *JHEP* **03**, 080 (2010) [arXiv:0911.1120 [hep-ph]].
- [122] N. Aghanim *et al.* [Planck], “*Planck 2018 results. VI. Cosmological parameters*,” *Astron. Astrophys.* **641**, A6 (2020) [erratum: *Astron. Astrophys.* **652**, C4 (2021)] [arXiv:1807.06209[astro-ph.CO]].
- [123] P. Gondolo and G. Gelmini, “*Cosmic abundances of stable particles: Improved analysis*,” *Nucl. Phys. B* **360**, 145-179 (1991)
- [124] L. Husdal, “*On Effective Degrees of Freedom in the Early Universe*,” *Galaxies* **4**, no.4, 78 (2016) [arXiv:1609.04979 [astro-ph.CO]].
- [125] K. Saikawa and S. Shirai, “*Primordial gravitational waves, precisely: The role of thermodynamics in the Standard Model*,” *JCAP* **05**, 035 (2018) [arXiv:1803.01038 [hep-ph]].
- [126] K. Saikawa and S. Shirai, “*Precise WIMP Dark Matter Abundance and Standard Model Thermodynamics*,” *JCAP* **08**, 011 (2020) [arXiv:2005.03544 [hep-ph]].
- [127] B. V. Lehmann and S. Profumo, “*Cosmology and prospects for sub-MeV dark matter in electron recoil experiments*,” *Phys. Rev. D* **102**, no.2, 023038 (2020) [arXiv:2002.07809 [hep-ph]].
- [128] H. H. Patel, “*Package-X: A Mathematica package for the analytic calculation of one-loop integrals*,” *Comput. Phys. Commun.* **197**, 276-290 (2015) [arXiv:1503.01469 [hep-ph]].
- [129] A. Denner, S. Dittmaier and L. Hofer, “*Collier: a fortran-based Complex One-Loop Library in Extended Regularizations*,” *Comput. Phys. Commun.* **212**, 220-238 (2017) [arXiv:1604.06792 [hep-ph]].
- [130] Y. Gong and X. Chen, “*Cosmological Constraints on Invisible Decay of Dark Matter*,” *Phys. Rev. D* **77**, 103511 (2008) [arXiv:0802.2296 [astro-ph]].
- [131] S. De Lope Amigo, W. M. Y. Cheung, Z. Huang and S. P. Ng, “*Cosmological Constraints on Decaying Dark Matter*,” *JCAP* **06**, 005 (2009) [arXiv:0812.4016 [hep-ph]].
- [132] B. Audren, J. Lesgourgues, G. Mangano, P. D. Serpico and T. Tram, “*Strongest model-independent bound on the lifetime of Dark Matter*,” *JCAP* **12**, 028 (2014) [arXiv:1407.2418 [astro-ph.CO]].
- [133] V. Poulin, P. D. Serpico and J. Lesgourgues, “*A fresh look at linear cosmological constraints on a decaying dark matter component*,” *JCAP* **08**, 036 (2016) [arXiv:1606.02073 [astro-ph.CO]].
- [134] G. F. Abellán, R. Murgia and V. Poulin, “*Linear cosmological constraints on 2-body decaying dark matter scenarios and robustness of the resolution to the  $S_8$  tension*,” [arXiv:2102.12498 [astro-ph.CO]].
- [135] J. F. Navarro, C. S. Frenk and S. D. M. White, “*The Structure of cold dark matter halos*,” *Astrophys. J.* **462**, 563-575 (1996) [arXiv:astro-ph/9508025 [astro-ph]].
- [136] J. F. Navarro, C. S. Frenk and S. D. M. White, “*A Universal density profile from hierarchical clustering*,” *Astrophys. J.* **490**, 493-508 (1997) [arXiv:astro-ph/9611107 [astro-ph]].
- [137] R. Laha, J. B. Muñoz and T. R. Slatyer, “*INTEGRAL constraints on primordial black holes and particle dark matter*,” *Phys. Rev. D* **101** (2020) no.12, 123514 [arXiv:2004.00627 [astro-ph.CO]].
- [138] R. Essig, E. Kuflik, S. D. McDermott, T. Volansky and K. M. Zurek, “*Constraining Light Dark Matter with Diffuse X-Ray and Gamma-Ray Observations*,” *JHEP* **11**, 193 (2013) [arXiv:1309.4091 [hep-ph]].
- [139] J. Y. Liao, S. Zhang, Y. Chen, J. Zhang, J. Jin, Z. Chang, Y. P. Chen, M. Y. Ge, C. C. Guo and G. Li, *et al.* “*Background model for the Low-Energy Telescope of Insight – HXMT*,” *JHEAp* **27**, 24-32 (2020) [arXiv:2004.01432 [astro-ph.IM]].
- [140] R. Krivonos, D. Wik, B. Grefenstette, K. Madsen, K. Perez, S. Rosslund, S. Sazonov and A. Zoglauer, “*NuSTAR measurement of the cosmic X-ray background in the 3–20 keV energy band*,” *Mon. Not. Roy. Astron. Soc.* **502**, no.3, 3966-3975 (2021) [arXiv:2011.11469 [astro-ph.HE]].
- [141] K. C. Y. Ng, B. M. Roach, K. Perez, J. F. Beacom, S. Horiuchi, R. Krivonos and D. R. Wik, “*New Constraints on Sterile Neutrino Dark Matter from NuSTAR M31 Observations*,” *Phys. Rev. D* **99**, 083005 (2019) [arXiv:1901.01262 [astro-ph.HE]].
- [142] D. E. Gruber, J. L. Matteson, L. E. Peterson and G. V. Jung, “*The spectrum of diffuse cosmic hard x-rays measured with heao-1*,” *Astrophys. J.* **520**, 124 (1999) [arXiv:astro-ph/9903492 [astro-ph]].
- [143] L. Bouchet, E. Jourdain, J. P. Roques, A. Strong, R. Diehl, F. Lebrun and R. Terrier, “*INTEGRAL SPI All-Sky View in Soft Gamma Rays: Study of Point Source and Galactic Diffuse Emissions*,” *Astrophys. J.* **679**, 1315 (2008) [arXiv:0801.2086 [astro-ph]].
- [144] L. Bouchet, A. W. Strong, T. A. Porter, I. V. Moskalenko, E. Jourdain and J. P. Roques, “*Diffuse emission measurement with INTEGRAL/SPI as indirect probe of cosmic-ray electrons and positrons*,” *Astrophys. J.* **739**, 29 (2011) [arXiv:1107.0200 [astro-ph.HE]].
- [145] The Hard X-ray Modulation Telescope (Insight-HXMT) website, <http://hxmtcn.ihep.ac.cn/mission.jhtml>.
- [146] H. Zhang *et al.* [PandaX], “*Dark matter direct search sensitivity of the PandaX-4T experiment*,” *Sci. China Phys. Mech. Astron.* **62**, no.3, 31011 (2019) [arXiv:1806.02229 [physics.ins-det]].
- [147] Y. Meng *et al.* [PandaX-4T], “*Dark Matter Search Results from the PandaX-4T Commissioning Run*,” *Phys. Rev. Lett.* **127**, no.26, 261802 (2021) [arXiv:2107.13438 [hep-ex]].

- [148] E. Aprile *et al.* [XENON], “*Projected WIMP sensitivity of the XENONnT dark matter experiment*,” *JCAP* **11**, 031 (2020) [[arXiv:2007.08796](#) [physics.ins-det]].
- [149] D. S. Akerib *et al.* [LZ], “*LUX-ZEPLIN (LZ) Conceptual Design Report*,” [[arXiv:1509.02910](#) [physics.ins-det]].
- [150] B. J. Mount, S. Hans, R. Rosero, M. Yeh, C. Chan, R. J. Gaitskell, D. Q. Huang, J. Makkinje, D. C. Mallin and M. Pangilinan, *et al.* “*LUX-ZEPLIN (LZ) Technical Design Report*,” [[arXiv:1703.09144](#) [physics.ins-det]].